Numerical Simulation for Dynamic Positioning in Pack Ice

by

©Jie Dai, B.Sc

A Thesis submitted to the School of Graduate Studies
in partial fulfillment of the requirements for
the degree of Master of Engineering

Faculty of Engineering and Applied Science

Memorial University of Newfoundland

May 2016

St. John's Newfoundland Canada

Abstract

This thesis investigates the numerical modelling of Dynamic Position (DP) in pack ice. A two-dimensional numerical model for ship-ice interaction was developed using the Discrete Element Method (DEM). A viscous-elastic ice rheology was adopted to model the dynamic behaviour of the ice floes. Both the ship-ice and the ice-ice contacts were considered in the interaction force. The environment forces and the hydrodynamic forces were calculated by empirical formulas. After the current position and external forces were calculated, a Proportional-Integral-Derivative (PID) control and thrust allocation algorithms were applied on the vessel to control its motion and heading.

The numerical model was coded in Fortran 90 and validated by comparing computation results to published data. Validation work was first carried out for the ship-ice interaction calculation, and former researchers' simulation and model test results were used for the comparison. With confidence in the interaction model, case studies were conducted to predict the DP capability of a sample Arctic DP vessel.

Acknowledgement

I would like to express my sincere gratitude to my supervisor, Dr. Heather Peng, for her continuous support, patience and guidance throughout the course of this thesis work. Her immense knowledge and kindly encouragement helped me all the time during this study.

I would also like to thank Dr. Wei Qiu, Dr. Claude Daley and Dr. David Molyneux for their valuable discussions and insightful advices.

This work was conducted at Memorial University of Newfoundland through fundings provided by NSERC CREATE Training Program for Offshore Technology Research (OTR). My sincere thank to MITACS Accelerate Internship Program for offering me the great internship opportunity.

My sincere thanks also goes to my senior fellow, Mr. Quan Zhou, who provided suggestions to and shared experiences with me at the beginning of my research. I thank my colleagues in the Advanced Marine Hydrodynamic Laboratory, for their support and company in the past two years.

My sincere appreciation goes to Mr. John Dolny and Mr. Dan Oldford of American Bureau of Shipping (ABS) for their professional guidance during my internship.

Last but not the least, I would like to thank my parents for supporting me spiritually throughout writing this thesis and my my life in general.

Table of Contents

List of Tables

List of Figures

List of Symbols

α	Orientation angle of a thruster
$\bar{f}$	Largest thrust value in T_{th}
β	Ship hull frame angle
Δt	Time step
ϵ	Difference between the circumradius and the inradius
μ	Ice friction coefficient
ϕ, θ, ψ	Vessel Euler angles in roll, pitch and yaw directions
ρ_{air}	Density of air
σ	Uniaxial compressive strength of ice
τ_c	The required net thrust for the ship demanded by the PID controller
τ_{PID}	The required control forces acting on the vessel in the global coordinate system
$\tilde{e}$	PID position error
φ	Polygon's central angle corresponding to one edge

ξ	Largest horizontal indentation
ξ_n	Largest normal indentation
A_c	Equivalent contact zone area
A_n	Normal contact area
$C_{Dx}^{\mathrm{w}}, C_{Dy}^{\mathrm{w}}, C_{Dn}^{\mathrm{w}}$	Drag coefficients for surge, sway and yaw motions
C_r	Freeze-bonding coefficient
C_{cf}	Cross flow drag coefficient
D_{ij}	Distance between centres of two ice floes during a collision
d_{nv}	Normal viscous damping coefficient
e	Current vessel position and heading $[x, y, \psi]^T$
e_d	Vessel position and heading set-point
F_n, F_t	Normal and tangent collision forces
F_{rv}	Remote viscous damping force
F_t^{p-1}	Tangential contact force in the previous time step
h_i	Ice floe thickness
I_x, I_y, I_z	Moments of inertia of the vessel with respect to x, y and z axes
I_{xy}, I_{xz}, I_{yz}	Products of inertia of the vessel
I_{yx}, I_{zx}, I_{zy}	Products of inertia of the vessel
J	Objective function

K, M, N	Moments about x, y and z directions
K_p, K_i, K_d	Proportional, integral and derivative gains of the PID controller
k_{ne}	Normal elastic coefficient
k_{rv}	Remote viscous damping coefficient
k_{te}	Tangent elastic coefficient
l_x, l_y	Lever arms of the thrusts
L_{ij}	Common chord of two ice floes during a collision
L_{pp}	Ship length between perpendiculars
m_x, m_y, m_ψ	Added mass of vessel of surge, sway and yaw motion
N	Number of polygon edges
n-t	Local coordinate system which is fixed on the ice floes
O-NED	Global coordinate system which is fixed on the earth surface
o-xyz	Local coordinate system which is fixed on the vessel
P	Power output of a thruster
p, q, r	Angular velicity about x, y and z directions
P_{min}, P_{max}	Minimum and maximum power output of a thruster
Q	Weighting matrix for the slack vector
R_i	Ice floe radius
s	Vector of slack variables

$t\%$	Error tolerance
T_a	Configuration matrix
T_x, T_y	Thrust components in x and y directions provided by a thruster
T_{max}	The maximum thrust
T_{min}	The minimum thrust
T_{th}	Summary matrix of thrusts from individual thrusters
u, v, w	Linear velocity in x, y and z directions
$u_{\mathrm{w}}, v_{\mathrm{w}}$	Wind velocity in x and y directions
v_{nr}, v_{tr}	Relative velocity of two objects in a collision in n and t directions
W	Quadratic weight matrix
$X(u)$	Water resistance on the vessel
X, Y, Z	Forces in x, y and z directions
x, y, z	Vessel positions in surge, sway and heave directions
X_C, Y_C, N_C	Control force components in 3DOF
X_E, Y_E, N_E	Environmental force components in 3DOF
x_g, y_g, z_g	Coordiantes of centre of gravity of the vessel with respect to o-xyz
X_H, Y_H, N_H	Hydrodynamic force components in 3DOF
X_I, Y_I, N_I	Ice induced force components in 3DOF

Chapter 1

Introduction

1.1 Background

With the Arctic region drawing increasing motivation and interest, Dynamic Positioning (DP) in ice has become a new challenge for the industry. The first DP system was developed in the 1960s, and later DP systems were applied to drilling ships and semi-submersibles in the 1970s. The practical purpose of equipping a ship with a DP system is to get better position keeping and course tracking, with optimized fuel consumption and minimized propulsion wear and tear. Nowadays DP systems have been widely installed in deep water drilling vessels, floating production vessels and ocean research and exploration vessels. However, DP operation in ice covered water is still a novel topic and demanding task.

Ice conditions can be defined based on a variety of criteria. Based on ice size, age, thickness and concentration, the ice can be classified into four primary types: broken ice, sheet ice, ridged ice and icebergs (Aboulazm & Muggeridge, 1989). A broken ice field, which is usually considered with relatively lower concentration and moderate

ice floe size, occurs more commonly than sheet and ridged ice in the marginal cold ocean. Before a drilling or exploration operation, ice breaking and management will be conducted by icebreakers. Therefore, DP operations mainly deal with pack ice with low concentration and relatively small size.

Ice conditions can significantly reduce the the capability of DP systems. When a vessel is transiting in ice floe covered water, one issue of particular interest is safety. Unlike the icebreaking process in level ice, the vessel will encounter occasional ice collisions in pack ice, especially when the ice concentration is low. Although the ice load is discrete and relatively low compared to icebreaking, a large number of interactions and peak values of the ice load still make a pack ice field a more complex environment than open water in terms of safety. The ice loads can be influenced by many factors, among which the principal ones are ice concentration, ice thickness, ice floe size, ship speed and hull shape.

In order to get a better understanding of ship-ice interaction and ship control in pack ice, many efforts have been made on model tests and full scale experiments. However, experimental studies on ship performance in ice are usually costly in terms of time, man power and financial expense. Furthermore, the available experimental data may not always be applicable for predictions of the in-ice performance of a new ship design. Therefore, a flexible and reliable numerical simulation for DP in pack ice is necessary for the analysis and predictions of vessels' performance and safety.

1.2 Literature Review

1.2.1 Interaction between Ship and Pack Ice

A few decades ago, most of the research effort and attention were concentrated on icebreaking and ship resistance in level ice, but only a few were devoted to pack ice. In recent years, due to the facts that large areas of water in the marginal zone of the Arctic Ocean are covered by pack ice, and most of the arctic commercial shipping activities are conducted in broken ice channels, the need for a better understanding of the mechanism behind ship-pack ice interaction becomes urgent. The literature review presented in this subsection is to collect and evaluate recent empirical, analytical, numerical and experimental studies on ship performance in pack ice.

1.2.1.1 Empirical and Analytical Study

Early experiences in the area of ship-pack ice interaction started mainly with empirical studies proposed by Russian researchers based on limited model tests or full-scale experiments. One of the first methods was suggested by Bronnikov (1959) and formulated from a model test of an arctic cargo ship. The relationship is indicated as follows,

$$R_i = 977F_r^{1.42}(\frac{D}{10920})^s(\frac{h}{0.8})^m(\frac{c}{0.8})^n(\frac{d}{7.3})^p(\frac{6.6}{L/B})^q(\frac{0.65}{C_b})^r(\frac{15B}{B_i})^k \times 2.4 \qquad (1.1)$$

where R_i is the ship resistance induced by the ice floes; D is the ship displacement; h is the ice floe thickness; c is the ice floe concentration; d is the ice floe length; L is the ship length; B is the ship beam; C_b is the block coefficient of the ship; B_i is the ice channel width; and s, m, n, p, q, r are empirical coefficients.

Buzuev and Ryvlin (1961) also suggested a formula based on model testing. And later from a field test program, the authors summarized another empirical relation for ice loads on ships moving through small and medium floes (Buzuev & Ryvlin, 1966). Kashteljan et al. (1969) divided the total ice resistance into four components: resistance induced by transferring inertia from the vessel to the ice floes, dissipative resistance from ice-ice and ice-water interactions, static resistance due to ice confinement, and open water resistance. Nozawa (1999) furthered the work of Kashteljan et al. (1969) by extending the approach to floating structures with complex geometry.

From the late 1970s to the 1980s, the U.S. Army Cold Regions Research and Enigneering Laboratory (CRREL) conducted several extensive full-scale tests of an icebreaker USCGC "Katmai Bay" moving through ice in the Great Lakes. Vance (1980) developed an empirical approach to predict ship resistance in brash ice based on the measurements from those tests. Greisman (1981) then used a 14 ft long model of the USCGC "Katmai Bay" for a model test and proposed another empirical relationship. During the same period, a number of other researchers also presented empirical studies on ship resistance in broken or pack ice fields (German et al., 1981; Gill et al., 1981; Eskola, 1983; Kitazawa & Ettema, 1986; Vinogradov, 1986).

Keinonen et al. (1996) and Keinonen and Robbins (1998) developed an approach that used existing level ice formulas to predict ship resistance in pack ice. In this approach, the authors estimated an "equivalent level ice thickness" of the broken ice field based on ice floe size, ice concentration, ice strength, snow cover, ice salinity and temperature. This estimated "equivalent level ice thickness" then can be substituted into equations formulated originally for level ice resistance calculation. One of the latest semi-empirical studies was presented in Croasdale et al. (2009), in which ice

floe size, ice thickness and ice confinement pressure were included to formulate the ice load. In the same year, Spencer and Molyneux (2009) derived formulas from a series of model tests with a bulbous bow, to predict the pack ice loads on moored vessels.

Aboulazm (1989) suggested that the empirical studies were mostly inadequate when applying to a different type of ship or different ice conditions. Moreover, Aboulazm (1989) indicated that some of the empirical coefficients or parameters from early Russian studies were difficult to obtain as they were not publicly available. Therefore, Aboulazm and Muggeridge (1989) and Aboulazm (1989) proposed two analytical models, the Micro Model and the Macro Model, to simulate ship resistance in pack ice. The Micro Model presumed a low ice concentration below 50% and moderate ship speed. Ice floes were treated as discrete elements and were driven towards the ship while assuming the ship to be fixed. Ship-ice interaction force was indirectly obtained by calculating the energy loss during the collision, as the energy loss would then be translated to an increase in ship resistance. The Macro Model took the same presumption of ice conditions and ship speed range as the Micro Model, while treating the ice field as continuous. By investigating the ice mechanics and dynamic properties, the ship-ice interaction force, which was continuous, could be calculated from ice motion and drag force.

1.2.1.2 Numerical Study

A discrete element method (DEM) was initially introduced by Cundall (1971) and Cundall and Strack (1979) to model materials assembled by independent interacting particles. The DEM was extended and applied to model the broken ice fields by Hopkins (1992). Since then, the applications of DEM have been widely conducted in Arctic Engineering.

Babić (1988) used a soft-particle approach to numerically simulate the granular material interaction behaviour. Contact forces were modelled in a viscoelastic rheology, where elastic and viscous property were considered. The approach was later adopted by Løset (1994a, 1994b) into a two-dimensional discrete element model of a broken ice field, where the ice floes were represented by circular discs to enhance computation efficiency. Hansen and Løset (1999a) extended the work of Løset (1994a) by introducing the concept of an "object", which enabled the simulation of ship-ice interaction. The simulation of a mooring turret was carried out by Hansen and Løset (1999b). Since then, this 2D DEM or analogous methods have been widely adopted and applied to simulations of different types of floating structures in broken ice fields. Karulin and Karulina (2011) studied the performance of a moored tanker in a field filled with ice floes changing drift direction. Lubbad and Løset (2011) conducted real-time simulations of ship-ice interaction by introducing a real-time physics engine called "PhysX". Furthermore, a 3-dimensional approach based on the DEM was suggested by Sawamura and Tachibana (2011) to simulate the interaction between the ice floes and the ship. The mechanism of the rotating and sliding motion of the ice floes was well modelled by this 3D approach.

Another popular technique of DEM for ice-related modelling is a commercial code called "DECICE", which was initially developed in the 1980s by Applied Mechanics Inc. and INTERA Technologies Inc. (Hocking et al., 1987), based on Williams et al. (1985). The original algorithm of DECICE was built to solve two structural mechanics problems, i.e., interaction between sea ice and offshore structures, and a discontinuous rock mass under traction controlled boundary conditions. DECICE was later owned by Oceanic Consulting Corporation (hereinafter to be referred to

as “Oceanic”) and also in use by NRC. It was further modified to several different sub-versions, respectively by those two organizations, in order to extend the code's versatility for particular problems in broken ice fields. DECICE has been extensively used by NRC and Oceanic to analyze structure-ice interactions for different types of simulations: ship manoeuvring in pack ice (Lau, 2006; Lau & Simões Ré, 2006; Zhan et al., 2010; Lau, 2011; Zhan & Molyneux, 2012), pack ice forces on drillships (Liu et al., 2010), moored tankers in pack ice (Murray & Spencer, 1997), ship performance in pack ice (McKenna et al., 1997; Quinton, 2006; Molyneux et al., 2012) and other ship-ice interaction problems (Lau et al., 2011).

One of the state-of-art DEM techniques in Arctic Engineering is a program called “GEM” (GPU-Event-Mechanics), which was proposed by Daley et al. (2012) to simulate local ice loads on vessels operating in pack ice. The GEM program extensively amplified the computational performance of DEM by employing GPU (Graphics Processing Unit) to do massively parallel programming. The background of computational techniques was demonstrated in Alawneh and Peters (2012) and Alawneh et al. (2015). A comprehensive statistical analysis of simulated pack ice loads was presented by Daley (2014).

Besides the DEM, a Particle-In-Cell (PIC) method was first proposed by Flato (1993) for sea ice forecasting, and later extended by Sayed and Carrieres (1999) and Zhang and Hibler (1997) to model ice-structure interactions. Several applications of the PIC method in broken ice fields have been conducted by the Nation Research Council of Canada (NRC) to calculate ice loads on floating structures, the drilling unit "Kulluk” (Barker et al., 2000a) and bridge piers (Barker et al., 2000b). The PIC method was also applied to examine damage zones and ice pile-up scenarios by Barker and Timco

(2003).

According to Wang et al. (2010), the PIC method is based on the concept that advects the material in a Lagrangian manner and then maps the information to a fixed Eulerian grid. The intact ice and bulk ice rubble are represented by discrete particles, which are assigned with information to describe the state of the ice cover, such as velocities, ice concentration and ice type. However, the discrete particles have no physical dimension and do not interact with each other. Instead, the particles are actually treated more as moving nodes that carry the information into the governing equations.

There are also limited applications of several other methods of ice-related modelling. The Smoothed Particle Hydrodynamics (SPH) method is used, although not widely, to simulate pack ice behaviour. Gutfraind and Savage (1998) used the SPH method to solve continuum equations for flow of fractured ice. Case studies of pack ice moving through a wedge-shaped channels were conducted, and simulation results were compared to DEM results. A finite element model (FEM) was proposed by Kim et al. (2013) to investigate the resistance performance of an icebreaker cargo vessel in pack ice conditions. The ship-ice interaction loads were numerically calculated based on a fluid structure interaction (FSI) method using the commercial FE package LS-DYNA. Simulation results were later validated by comparing them to model tests in a towing tank.

1.2.1.3 Experimental Study

(1) Full-Scale Tests

Full-scale field measurements have been conducted for a long time to evaluate ship

performance in ice. In the early stage, most of the sea trials were performed by icebreakers, but as interest in the Arctic increased, other types of ships and platforms were also involved in field measurements. Compared to level ice, it is much more difficult to control the pack ice field's characteristics, such as ice thickness, ice distribution and floe size, and it is usually time-consuming and expensive to saw a sheet ice into broken ice floes. Moreover, natural pack ice does not always meet the experiment setup requirement. Therefore, most of the measurements were conducted in level ice. Only a limited number of full-scale data in pack ice fields are in the public domain.

In 1979, The USCGC Icebreaker "Katmai Bay" was tested in brash ice conditions in Lake Superior to determine the operational capabilities of the vessel. The tests were conducted at different times of the year to get different thicknesses of the brash ice. Plots showing shaft power versus speed in different thicknesses of brash ice were presented by Vance (1980), and the shaft power data were also converted into ice resistance for regression analysis.

At the same time, because of the interest in the technical feasibility of navigation year round in Lake Melville, Labrador, two field trials were conducted with the CCGS Icebreaker "Sir John Franklin". The operational ice field was a mixture of brash ice, small ice floes and large ice floes in different concentrations, but the exact sizes of brash ice floes were not available. Ship thrusts measured for different ship speeds in various fragmented ice conditions were present by Michailidis and Murdey (1981).

The U.S. Coast Guard conducted the Winter 1992 Antarctic Tests of the "RV Nathaniel B. Palmer" (Schultz et al., 1994). Ship performance in open water, level ice and broken ice were all evaluated. The tests in broken ice were divided into two types of

tests. The first type was conducted in an unbounded broken ice field, while the second type was performed in a confined ice channel. The ice concentration of all tests was approximately 90%, while the ice thickness and snow cover thickness were varying. Pitch, thrust, RPM, torque, shaft power and ship speed were measured during the test for analysis.

Wright (2000) reported a full scale pack ice load data base developed from station-keeping operations in the Beaufort Sea with the drilling unit "Kulluk". Various scatter plots of expected ice loads in managed pack ice conditions were presented.

(2) Model Tests

Compared to full-scale experiments, model tests are much more flexible regarding time consumption, financial cost and technical preparation. Therefore, experiments in model-scale have been continuously conducted by researchers from both academia and the industry.

Tatinclaux (1984) presented model tests of two model ships of the USCGC "Katmai Bay", with scale ratios 10 and 24, respectively. Although the main purpose of those tests was to predict level ice resistance and icebreaking performance, ship resistance in broken ice fields was also measured. The broken ice tests were conducted in four types of fields: undistributed broken channels, pre-sawn channels, brash-filled channels and unconfined brash. The ice field length was also varied, as well as the ship advance speed.

Ettema et al. (1986) conducted series of experiments to study pack ice resistance acting on two bows in different forms. Aboulazm (1989) conducted a series of tests

towing a 1:40 model of the CCGS Icebreaker "Franklin" through triangular pack ice in different concentrations and ice thicknesses. Ice resistance was measured at various ship advance speeds. Løset and Timco (1993) presented results of a model test in which a boom was towed along a tank filled with circular ice floes. Murray and Spencer (1996) tested a scale model of a semi-submersible and a monohull tanker in drifting pack ice to investigate the global ice loads on the mooring system. In the same period, a modelled Submerged Turret Loading concept (STL) was tested by Løset et al. (1998) to study the feasibility of the STL concept in level ice, broken ice and pressure ridges. Comfort et al. (1999) assembled an extensive set of ice model test data for floating and moored structures in level ice and pack ice.

1.2.2 Dynamic Positioning System

In the 1960s, the first DP system was introduced with Proportional-Integral-Derivative (PID) control algorithms and low-pass filters, to deal with the horizontal ship motions (surge, sway and yaw). In the 1970s, Balchen et al. (1976) proposed the advanced control in DP using Kalman Filter and optimal control theory. In the 1990s, various techniques of nonlinear DP control methods were introduced by different researchers. In the 2000s, Hespanha and Morse (2002) proposed a hybrid control theory and Blanke et al. (2003) proposed fault-tolerant control. A comprehensive review of the developing history of DP in open water can be found in Sørensen (2011).

Although DP applications in open water have already become a mature technique, the current experience of DP in ice-covered water is still limited. The first full-scale DP operation in pack ice is the Sakhalin diving in spring 1999 (Keinonen et al., 2000). The operation was performed by a type-B ice class vessel called "CSO Constructor" to support compression diving, and was supported by two icebreakers. The Arctic

Coring Expedition (ACEX) was later conducted in pack ice at the Lomonosov ridge in August 2004 (Keinonen et al., 2006). Recently in 2008, a coring operation was carried out at North East Greenland, in which an automated DP system was employed to keep the drillship's station (Rohlén, 2009).

For the recent numerical studies of DP in pack ice, Jenssen et al. (2009) used an open water DP simulator with external ice force input to simulate the process of station-keeping in ice. They also presented a series of ice load model test results. It was concluded that the DP control system, integrated with a robust ice management, is feasible to conduct safe and effective operations in the arctic regions. Millan and Wang (2011) presented a model test executed by IOT. In the model test, the ice floes were initially set to be still and the DP vessel was towed at a desired speed.

A European research and development project DYPIC (Dynamic Positioning in Ice) was initiated by Hamburg Ship Model Basin (HSVA) (Hals & Jenssen, 2012; Jenssen et al., 2012; Dal Santo & Jochmann, 2012). Kerkeni et al. (2013a) discussed the differences between environmental loads in open water and managed ice fields, and concluded that ice loads are much higher than the wind and current loads. They proposed two different simulation frameworks to verify the control laws for DP in open water and ice fields, respectively. Kerkeni et al. (2013b) proposed a methodology, which is different from the classic approach, for DP capability plots in ice. Haase et al. (2012) and Haase and Jochmann (2013) gave the description and summary of DP model tests carried by HSVA as part of the project DYPIC. Model test setup and ice conditions were demonstrated in Haase et al. (2012). Selected results of the model tests were presented in Haase and Jochmann (2013). Based on the model test results, further analysis and discussions were presented by Metrikin et al. (2013), Kjerstad

and Skjetne (2014), Kjerstad et al. (2015) and Metrikin et al. (2015).

1.3 Thesis Objectives and Outline

The scope of this thesis includes the development of a discrete element method to model the ship-pack ice interaction and a numerical simulator for DP in pack ice. The main objectives of this thesis include:

- To develop a 3 degrees of freedom (DOF) time-domain numerical model based on DEM that is feasible to predict the ship-pack ice interaction forces and the ice-ice interaction forces.
- To develop a DP control system for ships' stationkeeping in pack ice.
- To validate the numerical interaction model by comparing the simulation results to model tests and full-scale experiments.
- To investigate the ship resistance induced by pack ice and the DP capability in ice-covered water.
- To provide recommendations for further work.

The outline of the thesis is briefly listed as follows:

- Chapter 1 provides the introduction of the thesis' major topic and the literature review of the previous work.
- Chapter 2 presents the theoretical derivation and adopted formulas of the interaction numerical model, as well as the mathematical background and formulation of the motion equations.

- Chapter 3 demonstrates the control algorithm of the DP system, which mainly includes a PID controller and a thrust allocator. In addition, the numerical implementation of the control system is briefly discussed.
- Chapter 4 presents the simulation results and validations with experimental data, followed by data analysis and discussions.
- Chapter 5 concludes the thesis and give recommendations of future work.

Chapter 2

Numerical Model

2.1 Kinematics

2.1.1 Reference Frames

In this study, three different reference frames, i.e. one fixed global frame and two moving local frames, are introduced to describe the motions of vessels and ice floes. Figure 2.1 is the sketch of the three reference frames.

***NED*:** The Earth-fixed North-East-Down (*NED*) frame is usually used for the navigation in marine operations. The position and orientation of the vessel and the ice floes should be described in this frame. *NED* is defined as a tangent plane on the Earth surface. In the *NED* frame, the origin O is a fixed point in the tangent plane, the N axis points towards true North, the E axis points towards East, and the D axis points normal downwards the Earth surface (Fossen, 2011).

***BODY*:** The vessel-fixed o-xyz frame is a moving frame used to express the vessel's linear and angular velocities and accelerations, as well as forces and moments acting

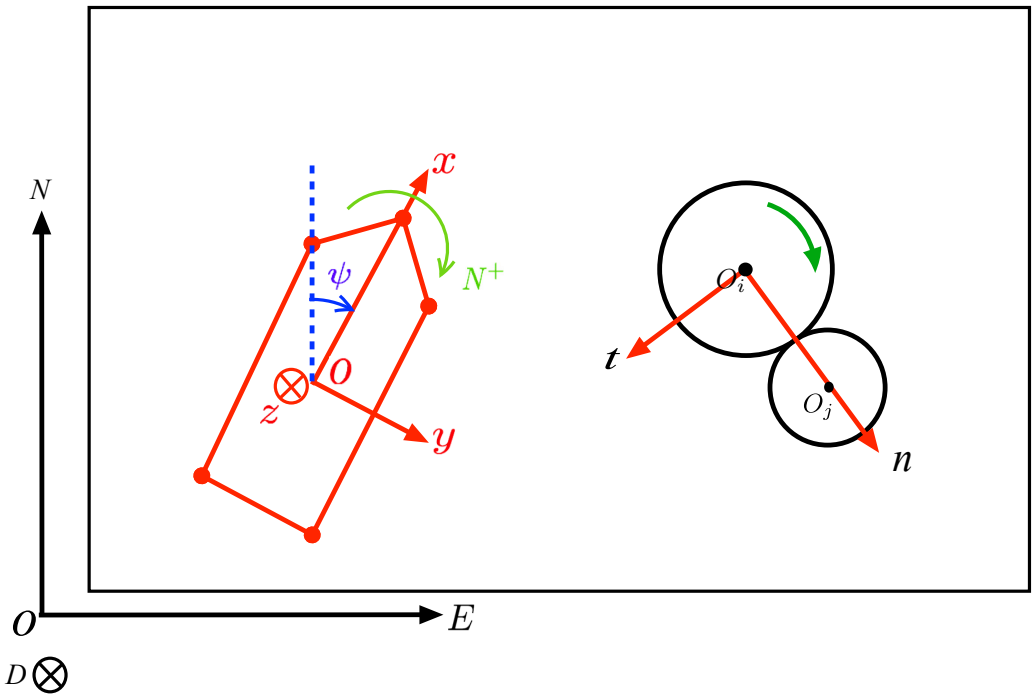

Figure 2.1: Sketch of the reference frames

on the vessel. In o-xyz, the origin o is the centre of the vessel waterplane. x is the longitudinal axis directing from stern to bow, y is the transversal axis directing from port to starboard, and z is the normal axis directing from top to bottom.

***ICE*:** Other than the vessel-fixed frame, the ice-fixed n-t reference frame is located along with each collision incident to express and calculate motions and forces involved in the ship-ice and the ice-ice interactions. n is the normal axis and t is the tangent axis. As presented in Fig. 2.1, for an ice-ice collision, the n axis is pointing from the centre of ice i to the centre of ice j, and the t axis is perpendicular to n. Though, the origin and the specific directions of the axes depend on the collision scenario, as the collision incident will be complicated if the ship and the ice are both involved.

2.1.2 Motion Variables and Notations

To discuss the vessel motions in 6 DOF, six independent coordinates are necessary to determine the vessel's position and orientation. The first three coordinates and their time derivatives represent the position and translational motion along the x, y and z axes, while the last three coordinates and their time derivatives denote the orientation and rotational motion.

Table 2.1: Notation of SNAME (1952) for marine vessels

DOF		Forces and moments	Linear and rotational velocities	Position and Euler angles
1	motion in x axis (surge)	X	u	x
2	motion in y axis (sway)	Y	v	y
3	motion in z axis (heave)	Z	w	z
4	rotation about x axis (roll)	K	p	ϕ
5	rotation about y axis (pitch)	M	q	θ
6	rotation about z axis (yaw)	N	r	ψ

The notation of SNAME (1952) for marine vessels is adopted in this study. Based on the motion variables listed in Table. 2.1, the vectorial notation of 6 DOF motion can be denoted as follows (Fossen, 1994):

$$\boldsymbol{\eta} = [\boldsymbol{\eta_1}^T, \boldsymbol{\eta_2}^T]^T; \quad \boldsymbol{\eta_1} = [x, y, z]^T; \quad \boldsymbol{\eta_2} = [\phi, \theta, \psi]^T$$
$$\boldsymbol{\nu} = [\boldsymbol{\nu_1}^T, \boldsymbol{\nu_2}^T]^T; \quad \boldsymbol{\nu_1} = [u, v, w]^T; \quad \boldsymbol{\nu_2} = [p, q, r]^T$$
$$\boldsymbol{\tau} = [\boldsymbol{\tau_1}^T, \boldsymbol{\tau_2}^T]^T; \quad \boldsymbol{\tau_1} = [X, Y, Z]^T; \quad \boldsymbol{\tau_2} = [K, M, N]^T$$

2.1.3 Coordinate System Transformations

The rate of the vessel's path change can be obtained by transforming the vessel's translational and rotational velocities from the vessel-fixed frame to the global frame.

This transformation from *BODY* to *NED* is denoted in the following vectorial form:

$$\dot{\boldsymbol{\eta}} = \boldsymbol{J}(\boldsymbol{\eta_2}) \cdot \boldsymbol{\nu} \tag{2.1}$$

The full expression of the transformation law in Eq. 2.1 is given by:

$$\begin{Bmatrix} \dot{x} \\ \dot{y} \\ \dot{z} \\ \dot{\phi} \\ \dot{\theta} \\ \dot{\psi} \end{Bmatrix} = \begin{bmatrix} c\psi c\theta & -s\psi c\theta + c\psi s\theta s\phi & s\psi s\theta + c\psi c\phi s\theta & 0 & 0 & 0 \\ s\psi c\theta & c\psi c\phi + s\psi s\theta s\theta & -c\psi s\theta + s\psi s\phi c\theta & 0 & 0 & 0 \\ -s\theta & c\theta s\phi & c\theta c\phi & 0 & 0 & 0 \\ 0 & 0 & 0 & 1 & s\theta t\theta & c\phi t\theta \\ 0 & 0 & 0 & 0 & c\phi & -s\phi \\ 0 & 0 & 0 & 0 & s\phi c\theta & c\phi c\theta \end{bmatrix} \begin{Bmatrix} u \\ v \\ w \\ p \\ q \\ r \end{Bmatrix} \tag{2.2}$$

where $s\cdot = \sin(\cdot), c\cdot = \cos(\cdot), t\cdot = \tan(\cdot)$.

In a 2-D model, only motions in the horizontal plane (surge, sway and yaw) are considered. Therefore, Eq. 2.2 can be simplified to Eq. 2.3.

$$\begin{Bmatrix} \dot{x} \\ \dot{y} \\ \dot{\psi} \end{Bmatrix} = \begin{bmatrix} \cos(\psi) & -\sin(\psi) & 0 \\ \sin(\psi) & \cos(\psi) & 0 \\ 0 & 0 & 1 \end{bmatrix} \begin{Bmatrix} u \\ v \\ r \end{Bmatrix} \tag{2.3}$$

The transformation matrix from *BODY* to *NED* is

$$\boldsymbol{R}(\psi) = \begin{bmatrix} \cos(\psi) & -\sin(\psi) & 0 \\ \sin(\psi) & \cos(\psi) & 0 \\ 0 & 0 & 1 \end{bmatrix} \tag{2.4}$$

Inversely, the transformation matrix from *NED* to *BODY* is

$$\boldsymbol{R}^{-1}(\psi) = \begin{bmatrix} \cos(\psi) & \sin(\psi) & 0 \\ -\sin(\psi) & \cos(\psi) & 0 \\ 0 & 0 & 1 \end{bmatrix} \tag{2.5}$$

The *ICE* frame is used to describe the ship-ice and the ice-ice collisions and calculate the interaction forces. The interaction forces should be transformed from *ICE* to *NED* for the ship-ice interactions, and to *BODY* for the ice-ice interactions. Denote α_{in} as the angle rotated from N axis to n axis, and α_{ib} as the angle rotated from x axis to n axis, then the transformation law can be formulated as

$$\boldsymbol{F_n} = \boldsymbol{R}(\alpha_{in}) \cdot \boldsymbol{F_i} \tag{2.6}$$

$$\boldsymbol{F_b} = \boldsymbol{R}(\alpha_{ib}) \cdot \boldsymbol{F_i} \tag{2.7}$$

where $\boldsymbol{F_n}$, $\boldsymbol{F_b}$, $\boldsymbol{F_i}$ are the 3 DOF forces and moments in *NED*, *BODY* and *ICE*, respectively. $\boldsymbol{R}(\alpha_{in})$ and $\boldsymbol{R}(\alpha_{ib})$ can be obtained as Eq. 2.4, only with ψ replaced by α_{in} and α_{ib}, respectively.

2.2 Ship Kinetics

2.2.1 Rigid-Body Equations of Motion

As presented in Figure 2.2, the vessel is considered as a rigid body in *BODY* with origin o. Since the *BODY* frame is moving with respect the inertial *NED* frame, ship kinetics in this study is discussed in the *BODY* frame.

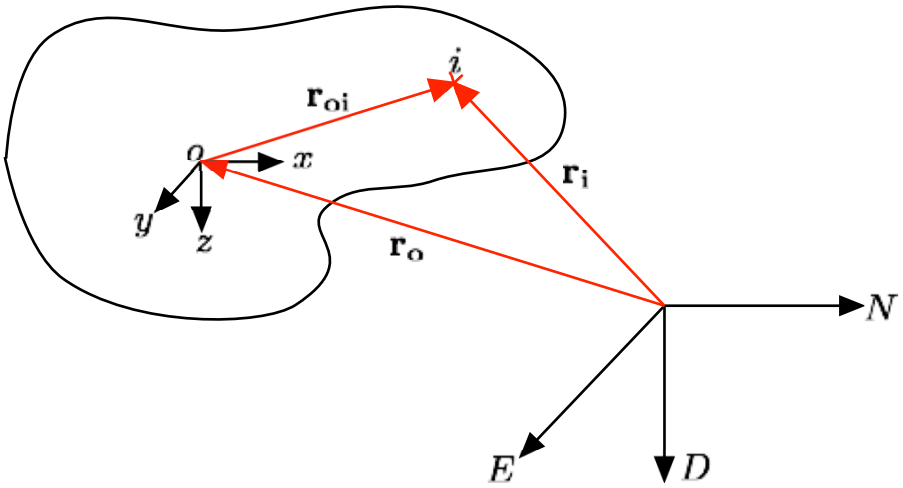

Figure 2.2: Rigid body sketch

2.2.1.1 Momentum of a Particle

According to Newton's second law, linear momentum for an arbitrary particle i obeys the following equality:

$$\boldsymbol{F}_i + \boldsymbol{R}_i = \frac{\mathrm{d}}{\mathrm{d}t}(m_i \boldsymbol{v}_i) \tag{2.8}$$

where $\boldsymbol{F}_i$ is the external forces acting on the particle and $\boldsymbol{R}_i$ is the internal forces exerted by the surrounding particles. The rigid body contains numerous of particles like i, and these particles are not moving apart or deforming. Therefore,

$$\sum_{i=1}^{S} \boldsymbol{R}_i = 0 \tag{2.9}$$

where S is the number of particles within the rigid body. Take the summation of Eq. 2.8 then we can get

$$\sum_{i=1}^{S} \boldsymbol{F}_i = \sum_{i=1}^{S} \frac{\mathrm{d}}{\mathrm{d}t}(m_i \boldsymbol{v}_i) \tag{2.10}$$

2.2.1.2 Linear Momentum in a Moving Frame

Consider an arbitrary particle i in Figure 2.2, the relationship between the radius vectors $\boldsymbol{r}_i$, $\boldsymbol{r}_o$ and $\boldsymbol{r}_{oi}$ is

$$\boldsymbol{r}_i = \boldsymbol{r}_o + \boldsymbol{r}_{oi} \tag{2.11}$$

Hence, the velocity of particle i is

$$\boldsymbol{v}_i = \dot{\boldsymbol{r}}_i = \dot{\boldsymbol{r}}_o + \dot{\boldsymbol{r}}_{oi} \tag{2.12}$$

By using the fact that $\dot{\boldsymbol{r}}_o = \boldsymbol{v}_o$ and $\dot{\boldsymbol{r}}_{oi} = \mathring{\boldsymbol{r}}_{oi} + \boldsymbol{\omega} \times \boldsymbol{r}_{oi}$,

$$\boldsymbol{v}_i = \boldsymbol{v}_o + \mathring{\boldsymbol{r}}_{oi} + \boldsymbol{\omega} \times \boldsymbol{r}_{oi} \tag{2.13}$$

where $\boldsymbol{v}_o$ is the velocity of the origin of $BODY$ frame, $\boldsymbol{\omega}$ is the angular velocity of the rigid body, $\mathring{\boldsymbol{r}}_{oi}$ is the time derivative of $\boldsymbol{r}_{oi}$ in $BODY$ frame and $\mathring{\boldsymbol{r}}_{oi} = 0$. Hence,

$$\boldsymbol{v}_i = \boldsymbol{v}_o + \boldsymbol{\omega} \times \boldsymbol{r}_{oi} \tag{2.14}$$

Substitute Eq. 2.14 into Eq. 2.10 to give

$$\begin{aligned} \sum_{i=1}^{S} \boldsymbol{F}_i &= \sum_{i=1}^{S} \frac{\mathrm{d}}{\mathrm{d}t}\Big[m_i \boldsymbol{v}_o + m_i(\boldsymbol{\omega} \times \boldsymbol{r}_{oi})\Big] \\ &= m\dot{\boldsymbol{v}}_o + \frac{\mathrm{d}}{\mathrm{d}t}\Big[\boldsymbol{\omega} \times \sum_{i=1}^{S}(m_i \boldsymbol{r}_{oi})\Big] \end{aligned} \tag{2.15}$$

Further define m as the mass of the rigid body and g as the centre of gravity of the rigid body such that

$$m = \sum_{i=1}^{S} m_i \tag{2.16}$$

$$m\boldsymbol{r}_{og} = \sum_{i=1}^{S}(m_i \boldsymbol{r}_{oi}) \tag{2.17}$$

Hence,

$$\begin{aligned}\sum_{i=1}^{S} \boldsymbol{F}_i &= m\Big[\dot{\boldsymbol{v}}_o + \frac{\mathrm{d}}{\mathrm{d}t}(\boldsymbol{\omega} \times \boldsymbol{r}_{og})\Big] \\ &= m\Big[\dot{\boldsymbol{v}}_o + \dot{\boldsymbol{\omega}} \times \boldsymbol{r}_{og} + \boldsymbol{\omega} \times \dot{\boldsymbol{r}}_{og}\Big] \\ &= m\Big[\dot{\boldsymbol{v}}_o + \dot{\boldsymbol{\omega}} \times \boldsymbol{r}_{og} + \boldsymbol{\omega} \times (\boldsymbol{\omega} \times \boldsymbol{r}_{og})\Big] \\ &= m\Big[\dot{\boldsymbol{v}}_o + \dot{\boldsymbol{\omega}} \times \boldsymbol{r}_{og} + \boldsymbol{\omega} \times (\boldsymbol{\omega} \times \boldsymbol{r}_{og})\Big]\end{aligned} \tag{2.18}$$

By using the vector triple product identity

$$\boldsymbol{\omega} \times (\boldsymbol{\omega} \times \boldsymbol{r}_{og}) = (\boldsymbol{\omega} \cdot \boldsymbol{r}_{og}) \cdot \boldsymbol{\omega} - (\boldsymbol{\omega} \cdot \boldsymbol{\omega}) \cdot \boldsymbol{r}_{og} \tag{2.19}$$

and the formula:

$$\dot{\boldsymbol{c}} = \mathring{\boldsymbol{c}} + \boldsymbol{\omega} \times \boldsymbol{c} \tag{2.20}$$

where $\dot{\boldsymbol{c}}$ and $\mathring{\boldsymbol{c}}$ are time derivatives of an arbitrary vector $\boldsymbol{c}$ in NED and $BODY$ frames, respectively, the previous derivation becomes

$$\boldsymbol{F} = \sum_{i=1}^{S} \boldsymbol{F}_i = m\Big[\mathring{\boldsymbol{v}}_o + \boldsymbol{\omega} \times \boldsymbol{v}_o + \mathring{\boldsymbol{\omega}} \times \boldsymbol{r}_{og} + (\boldsymbol{\omega} \cdot \boldsymbol{r}_{og}) \cdot \boldsymbol{\omega} - (\boldsymbol{\omega} \cdot \boldsymbol{\omega}) \cdot \boldsymbol{r}_{og}\Big] \tag{2.21}$$

According to the notation in Table 2.1, the vectors in Eq. 2.21 can be expressed in the $BODY$ frame as follows:

$$\boldsymbol{v}_o = \{u, v, w\} \tag{2.22}$$

$$\boldsymbol{r}_{og} = \{x_g, y_g, z_g\} \tag{2.23}$$

$$\boldsymbol{\omega} = \{p, q, r\} \tag{2.24}$$

$$\boldsymbol{F} = \{X, Y, Z\} \tag{2.25}$$

Substitute into Eq. 2.21, we then get three linear momentum equations:

$$\begin{aligned} X &= m[\dot{u} - vr + wq - x_g(q^2 + r^2) + y_g(pq - \dot{r}) + z_g(pr + \dot{q})] \\ Y &= m[\dot{v} - wp + ur - y_g(r^2 + p^2) + z_g(qr - \dot{p}) + x_g(qp + \dot{r})] \\ Z &= m[\dot{w} - uq + vp - x_g(p^2 + q^2) + x_g(rp - \dot{q}) + y_g(rq + \dot{p})] \end{aligned} \tag{2.26}$$

2.2.1.3 Angular Momentum

For angular momentum, the particle i obeys the following equality

$$\text{Total Moment} = \sum_{i=1}^{S} \Big[\boldsymbol{r}_{oi} \times \frac{\mathrm{d}}{\mathrm{d}t}(m_i \boldsymbol{v}_i) \Big] \tag{2.27}$$

Similar to the derivation of linear momentum, we have

$$\begin{aligned} \text{Total Moment} &= \sum_{i=1}^{S} \Big[m_i \boldsymbol{r}_{oi} \times \frac{\mathrm{d}}{\mathrm{d}t}(\boldsymbol{v}_o + \boldsymbol{\omega} \times \boldsymbol{r}_{oi}) \Big] \\ &= \sum_{i=1}^{S} \Big[m_i \boldsymbol{r}_{oi} \times (\dot{\boldsymbol{v}}_o + \dot{\boldsymbol{\omega}} \times \boldsymbol{r}_{oi} + \boldsymbol{\omega} \times \dot{\boldsymbol{r}}_{oi}) \Big] \\ &= \sum_{i=1}^{S} \Big[m_i \boldsymbol{r}_{oi} \times (\mathring{\boldsymbol{v}}_o + \boldsymbol{\omega} \times \boldsymbol{v}_o + \mathring{\boldsymbol{\omega}} \times \boldsymbol{r}_{oi} + \boldsymbol{\omega} \times (\boldsymbol{\omega} \times \boldsymbol{r}_{oi})) \Big] \\ &= m \boldsymbol{r}_{og} \times (\mathring{\boldsymbol{v}}_o + \boldsymbol{\omega} \times \boldsymbol{v}_o) + \sum_{i=1}^{S} \Big[m_i \boldsymbol{r}_{oi} \times (\mathring{\boldsymbol{\omega}} \times \boldsymbol{r}_{oi}) \Big] + \\ &\quad \sum_{i=1}^{S} \Big[m_i \boldsymbol{r}_{oi} \times (\boldsymbol{\omega} \times (\boldsymbol{\omega} \times \boldsymbol{r}_{oi})) \Big] \end{aligned} \tag{2.28}$$

The second term expands as

$$\begin{aligned}
\sum_{i=1}^{S}\Big[m_i\boldsymbol{r}_{oi}\times(\mathring{\boldsymbol{\omega}}\times\boldsymbol{r}_{oi})\Big] &= \sum_{i=1}^{S} m_i\Big[(\boldsymbol{r}_{oi}\cdot\boldsymbol{r}_{oi})\cdot\mathring{\boldsymbol{\omega}}-(\mathring{\boldsymbol{\omega}}\cdot\boldsymbol{r}_{oi})\cdot\boldsymbol{r}_{oi}\Big] \\
&= \left\{\begin{array}{l} \sum_{i=1}^{S} m_i\Big[(y_i^2+z_i^2)\dot{p}-(y_i\dot{q}+z_i\dot{r})x_i\Big] \\ \sum_{i=1}^{S} m_i\Big[(x_i^2+z_i^2)\dot{q}-(x_i\dot{p}+z_i\dot{r})y_i\Big] \\ \sum_{i=1}^{S} m_i\Big[(x_i^2+y_i^2)\dot{r}-(x_i\dot{p}+y_i\dot{q})z_i\Big] \end{array}\right\} \\
&= \left\{\begin{array}{l} I_{xx}\dot{p}+I_{xy}\dot{q}+I_{xz}\dot{r} \\ I_{yy}\dot{q}+I_{xy}\dot{p}+I_{yz}\dot{r} \\ I_{zz}\dot{r}+I_{xz}\dot{p}+I_{yz}\dot{q} \end{array}\right\}
\end{aligned} \tag{2.29}$$

where $I_{xx}, I_{xy}, I_{xz}, I_{yy}, I_{yz}$, and I_{zz} are the components of the moment of inertia. The third term in Eq. 2.28 expands as

$$\begin{aligned}
\sum_{i=1}^{S}\Big[m_i\boldsymbol{r}_{oi}\times(\boldsymbol{\omega}\times(\boldsymbol{\omega}\times\boldsymbol{r}_{oi}))\Big] &= \sum_{i=1}^{S}\Big[m_i\boldsymbol{r}_{oi}\times((\boldsymbol{\omega}\cdot\boldsymbol{r}_{oi})\cdot\boldsymbol{\omega}-(\boldsymbol{\omega}\cdot\boldsymbol{\omega})\cdot\boldsymbol{r}_{oi})\Big] \\
&= \sum_{i=1}^{S}\Big[m_i\boldsymbol{r}_{oi}\times\boldsymbol{\omega}\cdot(\boldsymbol{\omega}\cdot\boldsymbol{r}_{oi})\Big] \\
&= \left\{\begin{array}{l} \sum_{i=1}^{S} m_i(y_ir-z_iq)(x_ip+y_iq+z_ir) \\ \sum_{i=1}^{S} m_i(z_ip-x_ir)(x_ip+y_iq+z_ir) \\ \sum_{i=1}^{S} m_i(x_iq-y_ip)(x_ip+y_iq+z_ir) \end{array}\right\} \\
&= \left\{\begin{array}{l} I_{yz}(q^2-r^2)+I_{xz}pq-I_{xy}pr+(I_{zz}-I_{yy})rq \\ I_{xz}(r^2-p^2)+I_{xy}rq-I_{yz}pq+(I_{xx}-I_{zz})rp \\ I_{xy}(p^2-q^2)+I_{yz}pr-I_{xz}qr+(I_{yy}-I_{xx})qp \end{array}\right\}
\end{aligned} \tag{2.30}$$

According to the notation in Table 2.1, the total moment acting on the ship can be expressed as $\{K, M, N\}$. Substitute Eq. 2.29 and Eq. 2.30 into Eq. 2.28, the complete equations for

the angular momentum are formulated as:

$$\begin{aligned}
K &= I_{xx}\dot{p} + (I_{zz} - I_{yy})qr - (\dot{r} + pq)I_{xz} + (r^2 - q^2)I_{yz} + (pr - \dot{q})I_{xy} \\
&\quad + m[y_g(\dot{w} - uq + vp) - z_g(\dot{v} - wp + ur)] \\
M &= I_{yy}\dot{q} + (I_{xx} - I_{zz})rp - (\dot{p} + qr)I_{xy} + (p^2 - r^2)I_{xz} + (qp - \dot{r})I_{yz} \\
&\quad + m[z_g(\dot{u} - vr + wq) - x_g(\dot{w} - uq + vp)] \\
N &= I_{zz}\dot{r} + (I_{yy} - I_{xx})pq - (\dot{q} + rp)I_{yz} + (q^2 - p^2)I_{xy} + (rq - \dot{p})I_{xz} \\
&\quad + m[x_g(\dot{v} - wp + ur) - y_g(\dot{u} - vr + wq)]
\end{aligned} \tag{2.31}$$

2.2.1.4 Simplifying to 3 DOF

The ship model in this study is a 3-DOF model and only motions in the horizontal plane (surge, sway and yaw) are considered. Therefore, the heave, pitch and roll motions can be neglected (such that $w = p = q = \dot{w} = \dot{p} = \dot{q} = 0$). The ship geometry is assumed to be symmetric about the y axis and the centre of gravity of the ship lies in the y axis ($y_g = z_g = 0$). Hence, the moment of inertia $I_{xy} = I_{yx} = I_{yz} = I_{zy} = 0$. With the above assumptions, the 3 DOF equations of motion are

$$\begin{aligned}
m(\dot{u} - vr - x_g r^2) &= X \\
m(\dot{v} + ur + x_g \dot{r}) &= Y \\
I_{zz}\dot{r} + mx_g(\dot{v} + ur) &= N
\end{aligned} \tag{2.32}$$

2.2.2 Force and Moments Decomposition

According to Gong (1993), the right hand side of Eq. 2.32 can be decomposed as follows:

$$\begin{aligned} X &= X_I + X_H + X_E + X_C \\ Y &= Y_I + Y_H + Y_E + Y_C \\ N &= N_I + N_H + N_E + N_C \end{aligned} \tag{2.33}$$

where the terms with subscripts I, H, E, C denote the ice induced force, the hydrodynamic forces and moments acting on the hull, the environmental forces and the control forces, respectively.

2.2.3 Ice Induced Force

When a ship is moving through a pack ice field, the ice resistance typically results from the hull-ice collisions. These collisions can be head-on ramming or ship glancing off the ice floe, depending on the impact location and the relative ship-ice motion.

An initial impact occurs when the ship hull collides with an ice floe. As the ship and the ice floe continue moving against each other, an indentation occurs to the ice floe and the ship hull deforms as well. As a result, the ice floe is crushed in the contact zone and the crushing process produces a resisting force. The kinetic energy in the collision system is partly absorbed by the progressive ice crushing, and partly transformed into potential energy stored in the form of elastic strains. At the end of the collision, the potential energy is released as the elastic strains recover (Cammaert & Muggeridge, 1988).

2.2.3.1 Ship-ice collision

In this study, the ship, as well as the domain boundary, is modelled as a polygon which contains vertices and edges like presented in Fig. 2.3. The ice floes are modelled in circular shapes for computation simplicity.

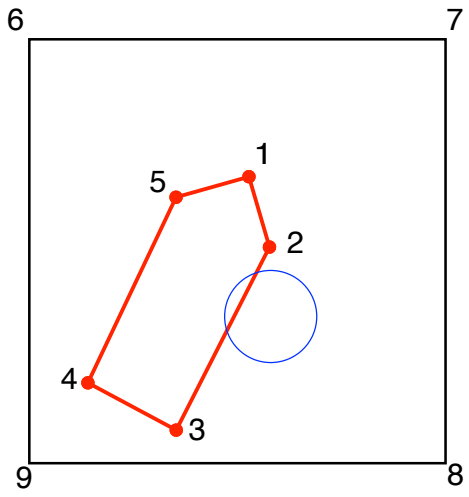

Figure 2.3: Elements in modelling

As most of the ship-ice collisions are momentary and the indented zone is very small compared to the ice floe's dimension, the indentation is represented by a 2D overlap of the ship hull and the ice floe in the simulation. Depending on the relative position of the ship hull and the ice floe, the ship-ice collision is classified into three scenarios as presented in Fig. 2.4:

- Scenario I: None of the nodes of the edge is within the circle;
- Scenario II: Only one node of the hull is within the circle;
- Scenario III: One or more nodes of the hull are within the circle.

For each collision scenario, the indentation ξ and the character chord of the overlap area L are calculated. For Scenario I, L is the intersected chord of the circle; for Scenario II and III, L is the segment between two points of intersection.

During the simulation, a collision search algorithm is conducted edge by edge for the ship. For one ship hull edge, the program searches potential collisions between the edge and the ice floes around the edge. Once a contact is detected between the hull edge and an ice floe, an ice-fixed n-t reference frame (the ICE frame) is established as presented in Fig. 2.5.

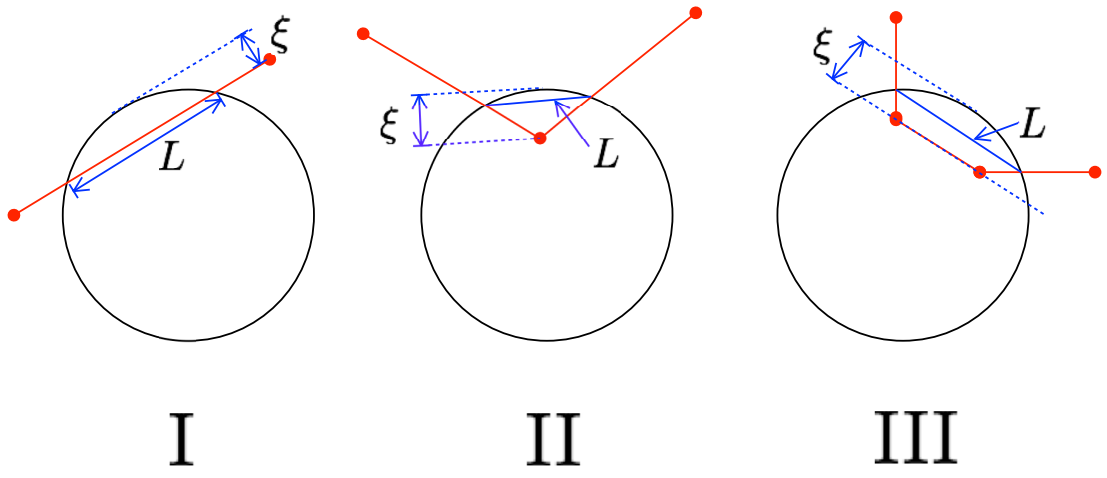

Figure 2.4: Ship-ice collision scenarios

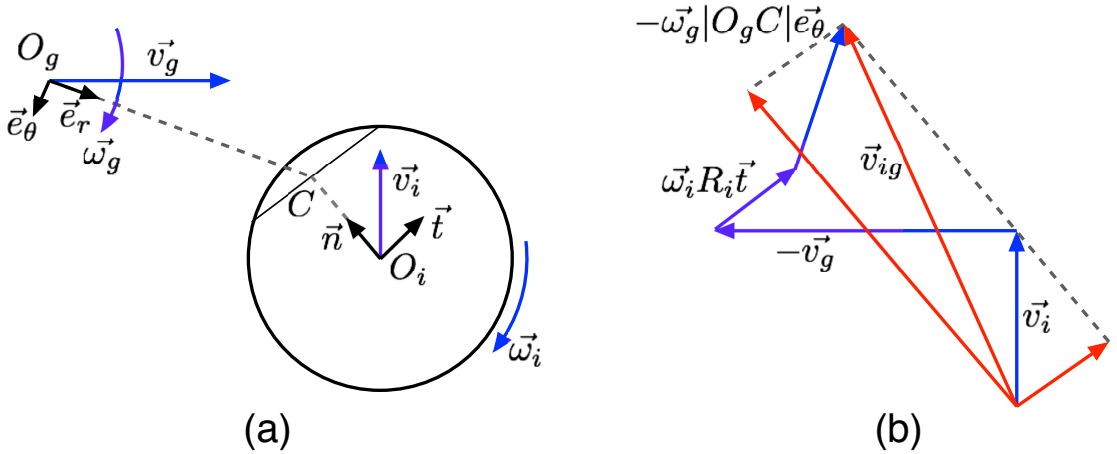

Figure 2.5: Collision sketch (a) 2D overlap; (b) Velocity vectors

In Fig. 2.5, O_g is the ship's centre of gravity. The ship has a linear velocity $\vec{v_g}$ and an angular velocity $\vec{\omega_g}$. O_i is the ice floe's centre of gravity and R_i is the radius of the floe. The ice floe has a linear velocity $\vec{v_i}$ and an angular velocity $\vec{\omega_i}$. Point C is the midpoint of the character chord and is taken as the point of contact. The n axis points from O_i to C. e_r and e_θ are the unit vectors of O_gC and its perpendicular, respectively. The ship-ice contact is detected if

$$|O_iC| \leq R_i \tag{2.34}$$

The 2D relative velocity at the point of contact can be calculated as follows:

$$\vec{V_{ig}} = \vec{v_i} - \vec{v_g} + \vec{\omega_i} \cdot R_i \cdot \vec{t} - \vec{\omega_g} \cdot |O_gC| \cdot \vec{e_\theta} \tag{2.35}$$

The 2D relative velocities in normal and tangential directions can be obtained by projecting the 2D relative velocities to the n-t unit axial vectors.

$$\begin{aligned} v_{nr} &= \vec{v}_{ig} \cdot \vec{n} \\ v_{tr} &= \vec{v}_{ig} \cdot \vec{t} \end{aligned} \tag{2.36}$$

2.2.3.2 Ship-ice interaction force

A viscous-elastic ice rheology is adopted in this study to model the forces resulted from ice impacts. Ice floes are treated as soft particles that can allow small deformation and indentation. However, flexural failure and compressive failure are neglected, and no ice breaking is assumed after collision.

In this method, the ice impact force is decomposed into the normal and tangent directions. As presented in Fig. 2.6, the normal component of the impact force is modelled as the sum of a viscous force (damping) and an elastic force (spring). For computation simplicity,

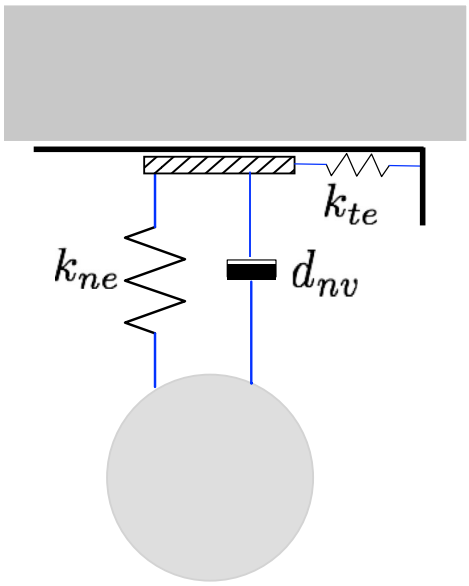

Figure 2.6: Impact force model sketch

the tangential component is modelled as an elastic force, and the shear friction effect is neglected. The viscous damping is to represent the energy dissipation in the ice crushing process, and the elastic spring is to represent the momentum transfer between the ship and the ice. The normal and tangent ship-ice interaction forces can be formulated as follows:

$$\begin{aligned} F_n &= -k_{ne} A_c - d_{nv} h_i v_{nr} \\ F_t &= F_t^{p-1} - k_{te} h_i v_{tr} \Delta t \end{aligned} \tag{2.37}$$

where F_n and F_t are the normal and tangent impact forces, respectively; k_{ne} and k_{te} are the normal and tangential elastic coefficients, respectively; d_{nv} is the normal viscous damping coefficient; F_t^{p-1} is the tangential contact force in the previous time step; A_c is the equivalent contact zone area in the horizontal direction; h_i is the ice floe thickness; v_{nr} and v_{tr} are the relative velocities at normal and tangential directions, respectively; and Δt is the time step.

(1) Contact zone area

The normal contact area increases as the ship crushes the ice floe and the resisting normal force steadily increases. The area of contact in a collision related to the indentation ξ, the character chord L, the ship hull frame angle β and the ice floe's size and thickness. As the real contact surface has complicated geometry in collision scenario II and III, two types of ideal contact surfaces are assumed, as presented in Fig. 2.7 and Fig, 2.8, for computation simplicity and efficiency (Zhou et al., 2016).

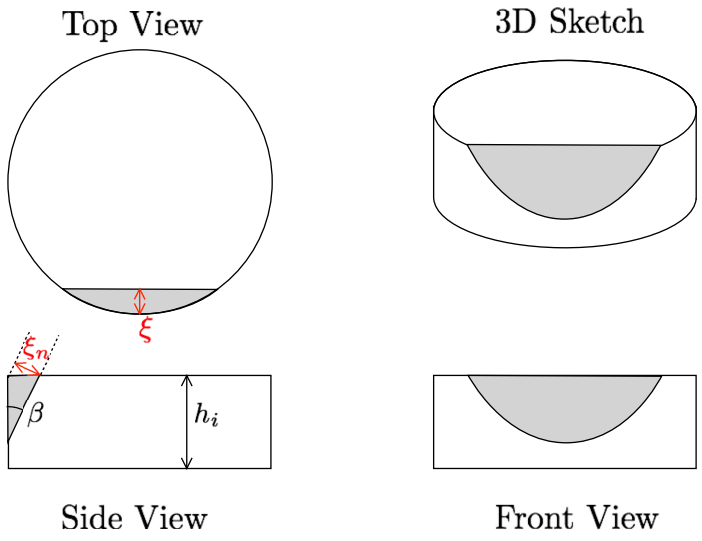

Figure 2.7: Ideal contact surface type 1

When the indentation is small, the contact surface is as illustrated in Fig. 2.7. The normal contact surface is in the shape of a segment. An analytical formula is suggested by Daley (1999) to calculate the normal contact surface area in Fig. 2.7. When a large indentation occurs and the indentation depth is larger than ice thickness, the normal contact surface is in a bowl-like shape as sketched in Fig. 2.8. For computation simplicity, the bowl-shaped contact surface is approximately represented by the shaded trapezoidal area in Fig. 2.8.

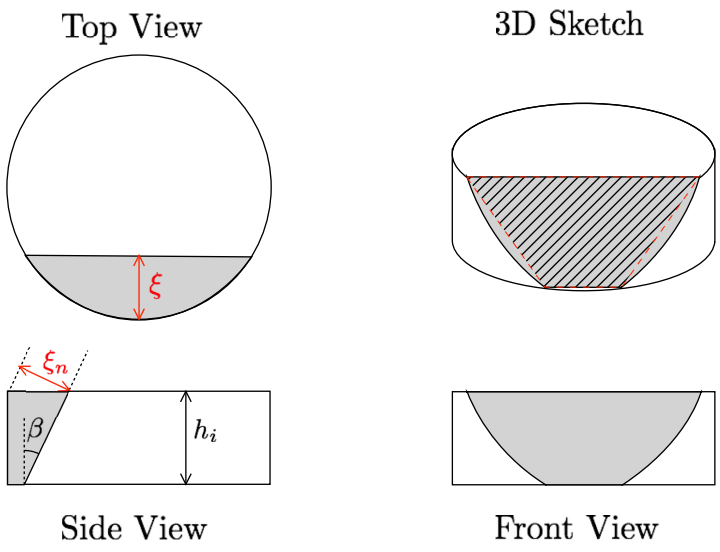

Figure 2.8: Ideal contact surface tpye 2

Therefore, the normal contact surface area can be calculated as follows:

$$An \begin{cases} = \dfrac{4}{3\sin\beta}\,\xi^{1.5}\sqrt{\dfrac{L^2}{4\xi}+\xi} & \text{if} \quad \xi \le h_i \tan\beta \\ \\ \approx \dfrac{h_i}{2\cos\beta}\Big[L+\sqrt{(\dfrac{L^2}{4\xi}+4h_i\tan\beta)(\xi-h_i\tan\beta)}\Big] & \text{if} \quad \xi > h_i\tan\beta \end{cases} \tag{2.38}$$

where A_n is the area of the normal contact zone; ξ is the largest horizontal indentation; L is the character width of the overlapped area; and β is the ship hull frame angle. Since the 2D model only considers motions and forces on the horizontal plane, the normal contact surface area A_n needs to be projected to the vertical plane to obtain the equivalent contact area A_c,

$$A_c = A_n \cos\beta \tag{2.39}$$

(2) Compressive limit

Compressive failure of ice is neglected in this model. Therefore, the normal contact force

F_n is controlled by a plastic limit (Løset, 1994a):

$$F_n = \begin{cases} F_n & \text{if} \quad |F_n| \leq \sigma A_c \\ \text{sign}(F_n) \cdot \sigma A_c & \text{if} \quad |F_n| > \sigma A_c \end{cases} \tag{2.40}$$

where σ is the uniaxial compressive strength of ice, sign(F_n) is the sign of F_n.

(3) Friction limit

The upper limit of the tangent contact force F_t is the Coulomb friction limit,

$$F_t = \begin{cases} F_t & \text{if} \quad |F_t| \leq \mu |F_n| \\ -\text{sign}(\ v_{tr}\ ) \cdot \mu |F_n| & \text{if} \quad |F_t| > \mu |F_n| \end{cases} \tag{2.41}$$

where μ is the hull-ice friction coefficient.

(4) Contact model coefficients

The contact model coefficients k_{ne}, k_{te} and d_{nv} are related to the momentum transfer and energy dissipation in the ice collisions. According to Hansen and Løset (1999a), knowing the magnitude of typical interaction force F, the magnitude of the normal elasticity k_{ne} can be approximately determined as follows:

$$k_{ne} \approx \frac{F}{1\% D h_i} \tag{2.42}$$

where D is the average ice floe diameter, and h_i is the average ice floe thickness. Eq. 2.42 is formulated by assuming only $1 \sim 2\%$ of the the average ice floe diameter is overlapped in a collision.

The tangential elastic coefficient k_{te} can be obtained as

$$k_{te} = \frac{k_{ne}}{2(1+\nu)} \tag{2.43}$$

where ν is the Poisson's ratio. Taking $\nu = 1/3$ (Mellor, 1986), k_{te} is obtained as $0.375k_{ne}$.

The normal viscous damping coefficient d_{nv} is set as a fraction of the critical damping,

$$d_{nv} = 2\,\xi_c\sqrt{mk_{ne}} \quad (0 \le \xi_c \le 1) \tag{2.44}$$

where m is the average ice floe mass, and ξ_c is the critical damping fraction factor. $\xi_c = 0$ indicates a perfectly elastic collision, while $\xi_c = 1$ indicates all energy is dissipated during a collision. In this study, ξ_c is taken as 0.9.

2.2.4 Hydrodynamic Force

The hydrodynamic forces are expressed as (Hirano, 1981):

$$\begin{aligned} X_H &= -m_x\dot{u} + X(u) + (m_y + X_{vr})vr \\ Y_H &= -m_y\dot{v} - Y_{\dot{r}}\dot{r} - m_x ur + Y_{H0} \\ N_H &= -m_\psi\dot{r} - N_{\dot{v}}\dot{v} + N_{H0} + Y_{H0}\cdot x_G \end{aligned} \tag{2.45}$$

where

$$\begin{aligned} Y_{H0} &= \frac{1}{2}\rho LT\left(Y_{uv}vU_0 + Y_{ur}rLU_0 + Y_{vr}v|r|L + Y_{vv}v|v| + Y_{rr}r|r|L^2\right) \\ N_{H0} &= \frac{1}{2}\rho L^2T\left(N_{uv}vU_0 + N_{ur}rLU_0 + N_{rr}r|r|L^2 + N_{vvr}v^2rL/U_0 + N_{vrr}vr^2L^2/U_0\right) \end{aligned}$$

where

$$X_{vr} = \frac{\partial X}{\partial v\partial r}, \quad Y_{uv} = \frac{\partial Y}{\partial u\partial v}, \quad N_{vvr} = \frac{\partial N}{\partial v^2\partial r}, \quad \cdots$$

are the hydrodynamic derivatives. ρ is the water density, L is the ship length, and T is the draft of the ship. $U_0 = \sqrt{u^2 + v^2}$ is the resultant velocity of the ship. $X(u)$ denotes the water resistance and can be calculated by Holtrop (1984). m_x, m_y and m_ψ are the surge, sway and yaw added mass of the vessel, respectively.

It is noteworthy that in case of dynamic positioning, the ship is in relatively low speed, and the hydrodynamic derivatives Y_{uv} and Y_{vv} used in high speed case should not be applied to calculate the lateral force Y_{H0}. For slow speed case, the cross flow drag force is introduced into Y_{H0}:

$$Y_{H0} = \frac{1}{2}\rho LT\left(C_{cf}U_0^2 \sin^2\beta + Y_{ur}rLU_0 + Y_{vr}v|r|L + Y_{rr}r|r|L^2\right)$$

where C_{cf} is the cross flow drag coefficient and β is the ship drift angle.

2.2.5 Environmental Force

2.2.5.1 Wind effect

The wind forces and moments acting on the ship can be estimated by various empirical formulas. In this study, the wind effect is calculated as follows (Peng & Spencer, 2008):

$$\begin{aligned} X_{\mathrm{w}} &= \frac{1}{2}\rho_{\mathrm{air}}C_{Dx}^{\mathrm{w}}L_{pp}^2|u_{\mathrm{w}} - u|(u_{\mathrm{w}} - u) \\ Y_{\mathrm{w}} &= \frac{1}{2}\rho_{\mathrm{air}}C_{Dy}^{\mathrm{w}}L_{pp}^2|v_{\mathrm{w}} - v|(v_{\mathrm{w}} - v) \\ N_{\mathrm{w}} &= \frac{1}{2}\rho_{\mathrm{air}}C_{Dn}^{\mathrm{w}}L_{pp}^3|v_{\mathrm{w}} - v|(v_{\mathrm{w}} - v) \end{aligned} \tag{2.46}$$

where u_{w} and v_{w} are the wind velocity projections on x and y axes, respectively. L_{pp} is the ship length between perpendiculars. ρ_{air} is the density of air. C_{Dx}^{w} and C_{Dy}^{w} are the drag coefficients on x and y axes, respectively. C_{Dn}^{w} is the drag coefficient for moment about z axis.

2.2.5.2 Current effect

According to Gong (1993), there are two approaches to account the current effect into the ship's motion equations. The first approach is to calculate the equivalent forces and moments induced by the current. The second approach is to use the ship speed relative to the current when calculating the hydrodynamic forces. The first approach is more realistic but more complex. The second approach assumes the steady state is reached and there is no relative motions due to the current. Considering the magnitude of the ice impact force is much larger than the current force in this study, the second approach is adopted for computation simplicity.

2.2.6 Control Force

In this study, instead of calculating the forces and moments generated by each thruster, propeller and rudder, the DP model employs a PID controller and a thrust allocation algorithm to obtain the control force. The detailed modelling of propellers and rudders is beyond the scope of this study, therefore, the command from the controller is assumed to be ideally reached by thrusters, considering thrust allocation algorithm applies limits and conditions to make the controller command as realistic as possible. Details of the control system modelling are discussed in Chapter 3.

2.3 Ice Kinetics

2.3.1 Equations of Motion

In a typical simulation of DP in pack ice, the number of ice floes can be up to thousands. Therefore, an adequately simple ice motion model is the key to the computation efficiency.

Explicit equations of motion as below are employed to describe the motion of the ice floes,

$$\begin{aligned}(m_i + m_{xi})\dot{v}_{xi} &= X_{Ii} + X_{Ei} \\ (m_i + m_{yi})\dot{v}_{yi} &= Y_{Ii} + Y_{Ei} \\ I_i\dot{\omega}_i &= N_{Ii} + N_{Ei}\end{aligned} \tag{2.47}$$

where m_i and I_i are the mass and moment of inertia of the ice floe, respectively; m_{xi} and m_{yi} are the added mass of ice in E and N directions, respectively; v_{xi} and v_{yi} are velocities of the ice floe in E axis and N axis, respectively; ω_i is the angular velocity of the ice floe in the global NED frame; and the terms with subscripts Ii and Ei denote the interaction and environmental forces and moments acting on the ice floe, respectively.

Same as the ship, only motions on the horizontal plane are considered for the ice. Different from the ship's equations of motion (Eq. 2.32), hydrodynamic effects on the ice are treated as added mass. Eq. 2.47 can be explicitly solved using a two-step Euler Method.

2.3.2 Ice-Ice Collision

Ice floes are modelled as soft particles in this method. During the simulation, by detecting the surrounding field, each ice-ice collision will be logged into the program. Then in each collision, a n-t coordinate system will be established and the ice motion information will be transformed into the n-t reference frame.

As presented in Fig. 2.9, two floes i and j are in a collision. The centres of the two floes are O_i and O_j, respectively. The linear velocities of the two floes are $\dot{O}_i$ and $\dot{O}_j$. The angular velocities of the two floes are ω_i and ω_j (taken positive in the counterclockwise direction). The n-t coordinate system is built with origin as O_i, defined by the following equations

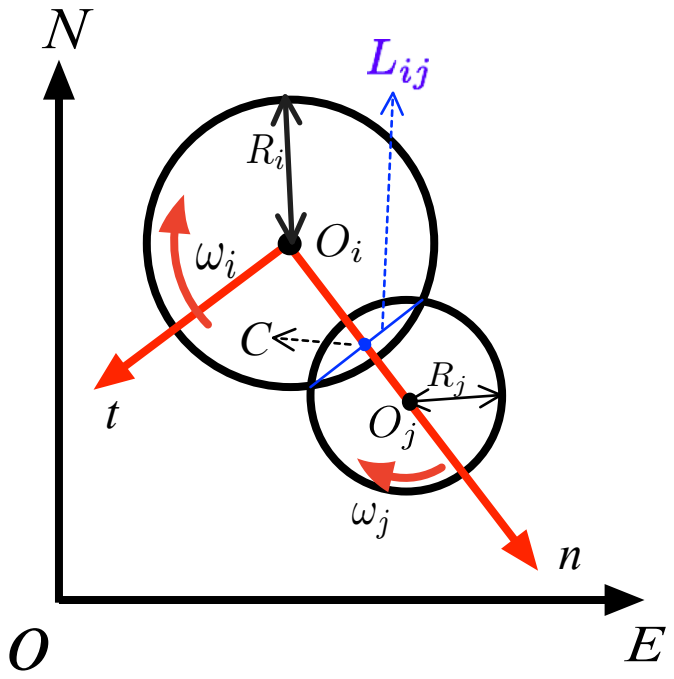

Figure 2.9: Ice-ice collision sketch

(Babić, 1988),

$$\vec{n} = \frac{\overrightarrow{O_iO_j}}{|O_iO_j|} = (\cos\theta, \sin\theta)$$
$$\vec{t} = (-\sin\theta, \cos\theta) \tag{2.48}$$

where $\vec{n}$, $\vec{t}$ are the unit vectors for the two axes.

The relative velocity at the point of contact C is given by

$$\dot{\overrightarrow{O_iO_j}} = \dot{O}_i - \dot{O}_j + (R_i\omega_i + R_j\omega_j)\vec{t} \tag{2.49}$$

where R_i and R_j are the radius of floes i and j, respectively. Then the relative displacement rates in the normal and tangential directions can be obtained by projecting the relative

velocity to the n-t unit axial vectors.

$$\begin{aligned} v_{nr} &= \dot{\overrightarrow{O_iO_j}} \cdot \vec{n} \\ v_{tr} &= \dot{\overrightarrow{O_iO_j}} \cdot \vec{t} \end{aligned} \tag{2.50}$$

2.3.3 Ice Interaction Force

The interaction force acting on the ice floes includes the ship-ice interaction force and the ice-ice interaction force. If one ice floe collides with the ship, the ship-ice interaction forces and moments acting on the ice floe will have the same value as the interaction forces and moments in Eq. 2.32, only with the opposite sign because of Newton's third law.

There are two types of ice-ice interaction force, primarily defined by the distance between two floes. When an actual overlap occurs between two floes, a solid contact will be logged in the program. Besides this situation, when two floes are close enough, even though without solid contact, there will be an interaction because of the freeze-bond with temperature below freezing. This freeze-bond is defined as a viscous force and logged as a "remote contact" force in the program when two floes have positive normal relative displacement rate (in compression) (Løset, 1994a).

For a solid contact, the principle for the calculation of the ice-ice interaction force in the normal and tangent directions is similar to the ship-ice collision. Eq. 2.37 is also used for ice-ice solid contact, only with different elastic and viscous coefficients and different contact surface area A_c. The ice floes are set to have uniform thickness and no vertical motion, therefore, the contact surface area for a ice-ice collision can be calculated by:

$$A_c = L_{ij} \cdot h_i \tag{2.51}$$

where L_{ij} is the common chord of the two floes, which can be calculated as follows:

$$L_{ij} = 2\sqrt{R_i^2 - \frac{(D_{ij}^2 + R_i^2 - R_j^2)^2}{4D_{ij}^2}} \tag{2.52}$$

where $D_{ij} = |O_i O_j|$.

The "remote contact" is logged into the simulation when

$$R_i + R_j < D_{ij} \leq (R_i + R_j)(1 + C_r) \tag{2.53}$$

where C_r is the freeze-bonding coefficient. The "remote contact" force is modelled as a weak viscous damping force in the normal direction, expressed as follows (Løset, 1994a):

$$F_{rn} = -k_{rv} \cdot h_i v_{nr} \tag{2.54}$$

where k_{rv} is the remote viscous damping coefficient.

2.3.4 Environmental Force

Both wind and current effects are considered for ice floes, which are calculated by the empirical formulas adapted from Peng and Spencer (2008). The wind force is:

$$\begin{aligned} X_{\mathrm{wi}} &= \frac{1}{2}\rho_{\mathrm{air}} C_{Dx}^{\mathrm{wi}} A_v |u_{\mathrm{w}} - v_{xi}|(u_{\mathrm{w}} - v_{xi}) \\ Y_{\mathrm{wi}} &= \frac{1}{2}\rho_{\mathrm{air}} C_{Dy}^{\mathrm{wi}} A_v |v_{\mathrm{w}} - v_{yi}|(v_{\mathrm{w}} - v_{yi}) \\ N_{\mathrm{wi}} &= 0 \end{aligned} \tag{2.55}$$

where u_{w} and v_{w} are the wind velocity projections on E and N axes, respectively. A_v is the projected area above water of ice. C_{Dx}^{wi} and C_{Dy}^{wi} are the drag coefficients on E and N axes for ice, respectively. C_{Dn}^{wi} is the drag coefficient for moment about D axis. The current

force is:

$$\begin{aligned} X_{\mathrm{ci}} &= \frac{1}{2}\rho_{\mathrm{water}} C_{Dx}^{\mathrm{ci}} A_v |u_{\mathrm{c}} - v_{xi}|(u_{\mathrm{c}} - v_{xi}) \\ Y_{\mathrm{ci}} &= \frac{1}{2}\rho_{\mathrm{water}} C_{Dy}^{\mathrm{ci}} A_v |v_{\mathrm{c}} - v_{yi}|(v_{\mathrm{c}} - v_{yi}) \\ N_{\mathrm{ci}} &= 0 \end{aligned} \tag{2.56}$$

where u_{c} and v_{c} are the current velocity projections on E and N axes, respectively.

Chapter 3

Dynamic Positioning System

3.1 System Diagram

The block diagram in Fig. 3.1 is a brief presentation of the DP controller system coupled with the ship model and the external force models. The ship model represents the motion equations. The ice model is the core part of the DEM program calculating and simulating the ship-ice and the ice-ice collisions. The wind and the hydrodynamic forces are calculated by the environment model. The DP controller system consists of the PID control command and the thrust allocation module.

During the simulation, the program detects the position and velocity information of the vessel and every ice floe at each time step. The position and velocity information are then delivered to the controller, as well as the external force models. Interaction incidents and contact types are determined based on the position and velocity information, then ice loads and the environmental forces are calculated by the ice model and the environment model, respectively. On the other hand, the PID controller takes the difference between the current position and the set-point as an input, then gives the thrust demand in surge, sway and yaw as the output. The thrust demand, which is the required thrusts for the vessel in 3 DOFs,

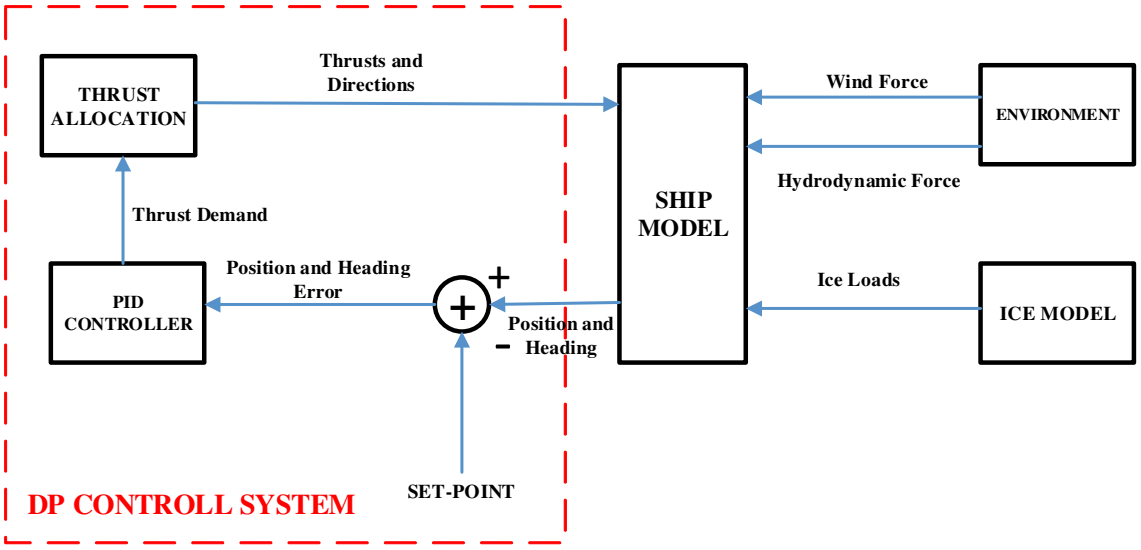

Figure 3.1: Block diagram of DP system

are allocated to each individual thruster by the allocation algorithm. In the end, the new position and velocity information at the next time step then can be obtained by solving the motion equations. Detailed demonstration of the DP control system is in the following subsections.

3.2 Control Force and Moment

The control force and moment $[X_C, Y_C, N_C]$ is the resultant force and moment provided by all thrusters. The force and moment provided by each thruster, i.e., the control command, is obtained by allocating the control demand to each thruster. The control demand is the required force and moment obtained from the PID controller based on the vessel's position and heading. The detailed modelling of the PID controller and the thrust allocator is demonstrated in the following sections.

3.3 PID Controller

The dominant external force, the ship-ice interaction force, is discrete and highly non-linear, therefore a PID control algorithm is developed to get the force command for the vessel to operate in the desired position and heading. In this PID controller, the position and heading error between the set-point and the actual value delivered from the ship model is taken as the input, and the thrust demands for surge, sway and yaw are the output. The principal control law is expressed as Eq. 3.1 (Fossen, 2011):

$$\tau_{\mathrm{PID}} = -K_p\tilde{e} - K_d\dot{\tilde{e}} - K_i\int_0^t \tilde{e}(\tau)d\tau \tag{3.1}$$

where K_p, K_i, K_d are the proportional, integral and derivative gains, respectively. Specifically in this study, τ_{PID} is the required control forces acting on the vessel in the global coordinate system,

$$\tau_{\mathrm{PID}} = [\tau_E, \tau_N, \tau_D]^T \tag{3.2}$$

where τ_E, τ_N and τ_D are the force commands in the O-NED reference frame, respectively. The position error $\tilde{e}$ is expressed as follows

$$\tilde{e} = e - e_d \tag{3.3}$$

where e represents the current vessel position and heading $[x, y, \psi]^T$, and e_d is the vessel position and heading set-point. $\dot{\tilde{e}}$ is the time derivative of $\tilde{e}$.

In order to get a better control response, three sets of PID gains are used in the program. For position control, when tracking error is large, larger K_p and smaller K_d will be adopted to speed up the response; otherwise when tracking error is within certain range, smaller K_p and larger K_d will be adopted to reduce the overshoot. For heading control, K_p, K_i and K_d are all larger than gains used in position control.

3.4 Thrust Allocation

3.4.1 Control Demand

Control demand τ_c is the required net thrust for the ship demanded by the PID controller. $\tau_c = [F_x, F_y, M_z]^T$ is in the ship-fixed o-xyz frame and it can be calculated as follows,

$$\begin{bmatrix} F_x \\ F_y \\ M_z \end{bmatrix} = \boldsymbol{R}^{-1}(\psi) \cdot \tau_{PID} = \boldsymbol{R}^{-1}(\psi) \cdot \begin{bmatrix} \tau_E \\ \tau_N \\ \tau_D \end{bmatrix} \tag{3.4}$$

where $\boldsymbol{R}^{-1}(\psi)$ is the transformation matrix from the earth-fixed NED frame to the ship-fixed $BODY$ frame (see Eq. 2.5); τ_{PID} is the command from the PID controller; F_x and F_y are the control demand force in the surge and sway directions, respectively; M_z is the demand moment in the yaw direction.

3.4.2 Actuator Models

The thrust provided by one individual actuator is projected to x and y axes in the ship-fixed frame and denoted as follows:

$$\boldsymbol{T} = \begin{bmatrix} T_x \\ T_y \end{bmatrix} \tag{3.5}$$

where T_x and T_y are the thrust components in x and y axis, respectively. If taking T_x and T_y as two axes of a 2D Cartesian coordinate system, a set of inequality constraints on $\boldsymbol{T}$ can define a limited and closed subset of $\mathbb{R}^2$. This subset of $\mathbb{R}^2$ is called "thrust region" and it represents a working area for a thruster. Usually the inequality constraints on $\boldsymbol{T}$ denote the thrust amount limit and and thrust direction limit. For different types of thrusters, the shape of the thrust region and the thrust constraints are different. As the conventional ducted propellers and rudders have been seldom adopted on modern DP vessels, only azimuth or tunnel actuators are modelled in this study.

3.4.2.1 Fixed thruster

A fixed thruster is a non-rotatable actuator with fixed orientation angle α. As illustrated in Fig. 3.2, the thrust region of a fixed thruster can be modelled as a line segment. T_{max} (≥ 0)

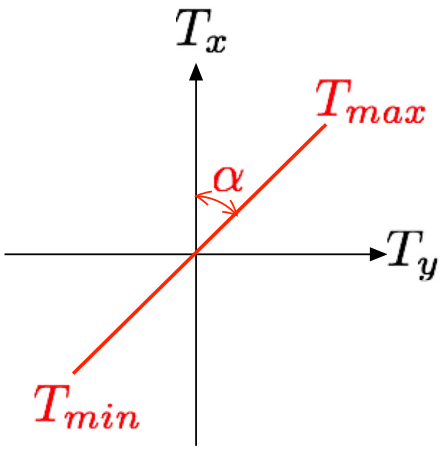

Figure 3.2: Schematic thrust region for a fixed thruster

and T_{min} (≤ 0) are the upper and lower limits of the thrust, respectively. The constraints can be mathematically expressed as follows,

$$\begin{bmatrix} \sin\alpha & -\cos\alpha \end{bmatrix} \cdot \begin{bmatrix} T_x \\ T_y \end{bmatrix} = 0 \tag{3.6}$$

$$\begin{bmatrix} \cos\alpha & \sin\alpha \\ -\cos\alpha & -\sin\alpha \end{bmatrix} \cdot \begin{bmatrix} T_x \\ T_y \end{bmatrix} \leq \begin{bmatrix} T_{max} \\ -T_{min} \end{bmatrix} \tag{3.7}$$

Specifically for a tunnel thruster, α is 90° and usually $T_{max} = -T_{min}$.

3.4.2.2 Azimuth thruster

An azimuth thruster is a rotatable thrust unit that can provide thrust in any direction on the horizontal plane (if no additional constraints). The thrust angle α can be obtained by

$$\alpha = \begin{cases} \arctan(T_y/T_x) & \text{if} \quad T_x > 0 \\ \pi + \arctan(T_y/T_x) & \text{if} \quad T_y \geq 0, T_x < 0 \\ -\pi + \arctan(T_y/T_x) & \text{if} \quad T_y < 0, T_x < 0 \\ \frac{\pi}{2} & \text{if} \quad T_y > 0, T_x = 0 \\ -\frac{\pi}{2} & \text{if} \quad T_y < 0, T_x = 0 \end{cases} \tag{3.8}$$

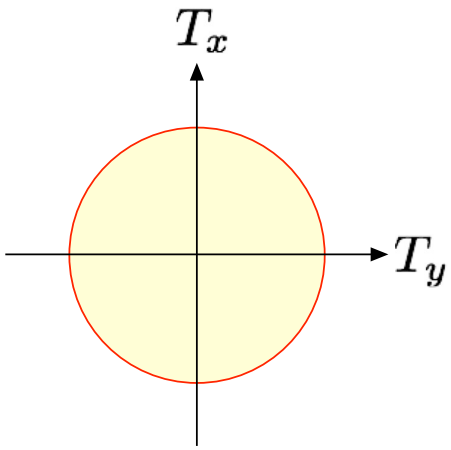

Figure 3.3: Schematic thrust region for an azimuth thruster

Providing that the azimuth thruster does not give reverse thrusts, the azimuth thruster has an upper limit $T_{max} > 0$ and a lower limit $T_{min} = 0$. As illustrated in Fig. 3.3, the thrust region for azimuth thrusters can be modelled as a circle with a radius equal to T_{max}, and the mathematical expression is

$$\sqrt{T_x^2 + T_y^2} \leq T_{max} \tag{3.9}$$

According to De Wit (2009), the non-linear inequality in Eq. 3.9 can be linearized by approximating the circle-shaped thrust region in Fig. 3.3 to a polygon. In order to avoid overrating the vessel's DP capability, the approximated thrust region should be strictly within the original thrust region. Therefore, an inscribed regular polygon of the circle is used as the approximation.

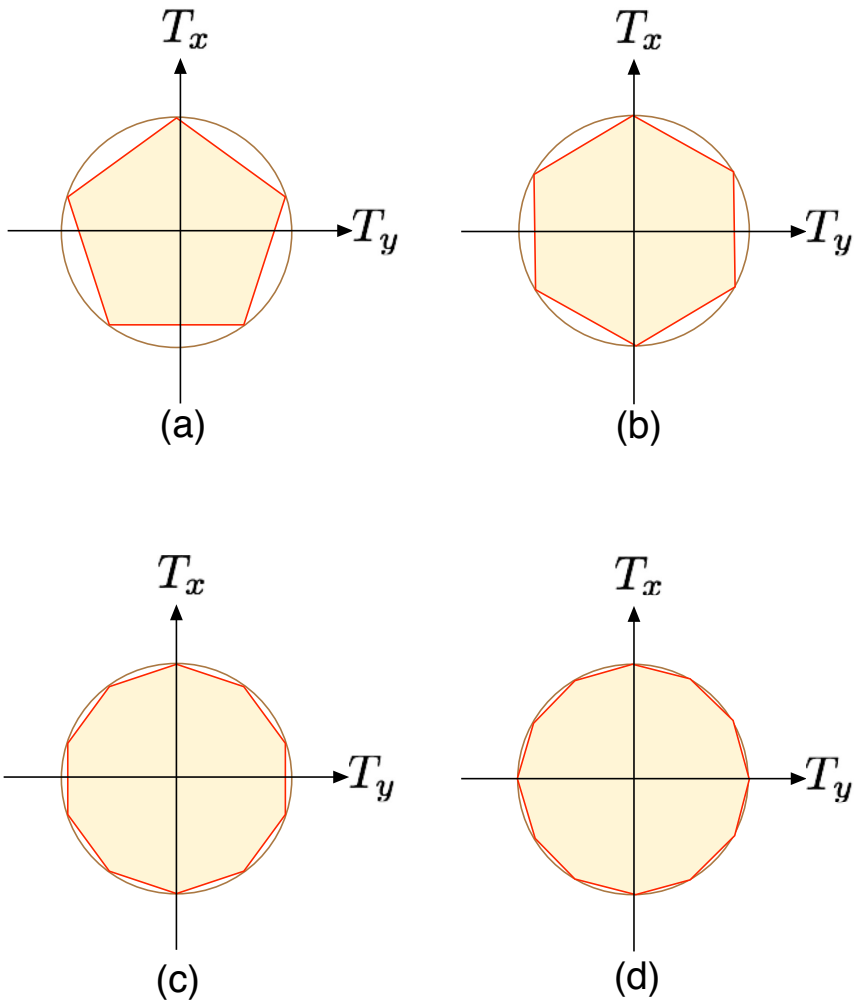

Figure 3.4: Schematic approximated polygon-shaped thrust region (a) N=5; (b) N=6; (c) N=10; (d) N=12

As illustrated in Fig. 3.4, the approximation accuracy increases as the number of polygon

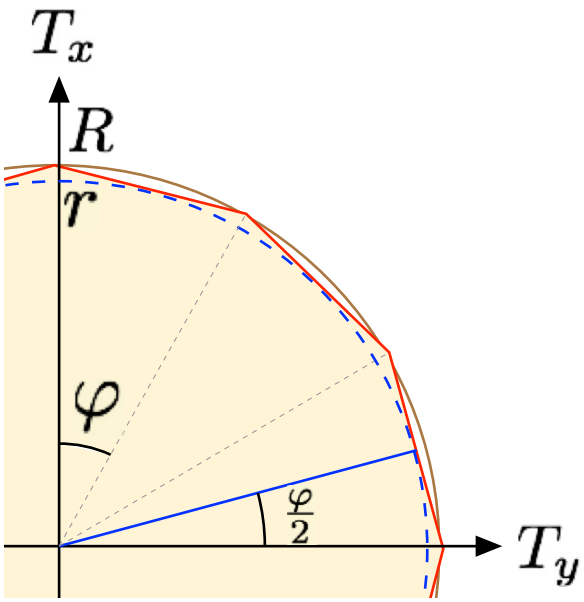

Figure 3.5: Sketch for approximation evaluation

edges N increases. For an inscribed regular polygon with N edges ($N \geq 3$) (see Fig. 3.5), the central angle corresponding to one edge is

$$\varphi = \frac{2\pi}{N} \tag{3.10}$$

Providing $T_{max} = R$ is the circumradius of the polygon, the polygon's inradius is

$$r = R\cos\left(\frac{\varphi}{2}\right) = R\cos\left(\frac{\pi}{N}\right) \tag{3.11}$$

According to De Wit (2009), the maximum error between the original and the approximated thrust region is the difference between the circumradius and the inradius:

$$\epsilon = R - r = R\left[1 - \cos\left(\frac{\pi}{N}\right)\right] \tag{3.12}$$

Therefore, if an error tolerance $t\% = (\frac{\epsilon}{R})_{max}$ is required, the following inequality can be derived from Eq. 3.12:

$$N \geq \frac{\pi}{\arccos(1 - t\%)} \tag{3.13}$$

After the edge number N defined, the linear inequality for the approximated polygon-shaped thrust region can be expressed as follows:

$$\begin{bmatrix} \cos\varphi_1 & \sin\varphi_1 \\ \cos\varphi_2 & \sin\varphi_2 \\ \vdots & \vdots \\ \cos\varphi_k & \sin\varphi_k \end{bmatrix} \cdot \begin{bmatrix} T_x \\ T_y \end{bmatrix} \leq r \tag{3.14}$$

where

$$\varphi_k = (2k+1)\frac{\pi}{N} \quad \text{with} \quad k = 0, \cdots, N-1 \tag{3.15}$$

3.4.3 Configuration Matrix

According to Millan (2008), the relationship between the control demand and the individual thruster demand is as follows:

$$\tau_c = T_a \cdot T_{th} \tag{3.16}$$

where T_a is the configuration matrix and T_{th} is the summary matrix of thrusts from individual actuators. The configuration matrix is used to transform the thrusts generated by individual thrusters to the total forces and moment on the ship. For an individual thruster thrusts $T = [T_x \ T_y]^T$, the forces and moment acting on the ship is calculated as follows:

$$\begin{bmatrix} 1 & 0 \\ 0 & 1 \\ -l_y & l_x \end{bmatrix} \cdot \begin{bmatrix} T_x \\ T_y \end{bmatrix} = \begin{bmatrix} F_x \\ F_y \\ M_z \end{bmatrix} \tag{3.17}$$

where l_x and l_y are the lever arms of the thrusts. Given the coordinates of the thruster in the ship-fixed frame as (x, y), and the ship's centre of gravity as (x_{cg}, y_{cg}),

$$\begin{aligned} l_x &= x - x_{cg} \\ l_y &= y - y_{cg} \end{aligned} \tag{3.18}$$

Providing there are n thrusters on the vessel, then $T_{th} \in \mathbb{R}^{2n}$ and $T_a \in \mathbb{R}^{3\times 2n}$,

$$T_{th} = \begin{bmatrix} T_{1x} & T_{1y} & T_{2x} & T_{2y} & \cdots & T_{nx} & T_{ny} \end{bmatrix}^T \tag{3.19}$$

$$T_a = \begin{bmatrix} 1 & 0 & 1 & 0 & \cdots & 1 & 0 \\ 0 & 1 & 0 & 1 & \cdots & 0 & 1 \\ -l_{1y} & l_{1x} & -l_{2y} & l_{2x} & \cdots & -l_{ny} & l_{nx} \end{bmatrix} \tag{3.20}$$

3.4.4 Allocation Objectives

The primary objective of the thrust allocator is to minimize the energy consumption of the propulsion system while fulfilling the overall control demand τ_c. The relationship between the individual actuator thrusts T_{th} and the energy consumption will be discussed in this subsection.

According to Leavitt (2009),

$$P = (P_{max} - P_{min})(\frac{|T|}{T_{max}})^{\eta} + P_{min} \tag{3.21}$$

where η is typically in the range of $(1.3, 1.7)$; P_{min} is the power output when $T = 0$ and P_{max} is the power output when $T = T_{max}$.

The value range of η is determined experimentally. In order to conveniently compute the allocation with quadratic programming, we can assume that $\eta \approx 2$, so that the energy

consumption P is directly proportional to a quadratic function,

$$P \propto (wT^2 + c) \tag{3.22}$$

where w and c are constants.

Based on the above approximation, the following quadratic objective function can be written in matrices:

$$J = \min_{T_{th}} \{T_{th}^T W T_{th}\} \tag{3.23}$$

where W is a positive diagonal matrix which contains quadratic weight constants w in Eq. 3.22.

3.4.5 Quadratic Programming

Quadratic programming (QP) is a mathematical optimization method for a quadratic function of variables subject to linear constraints (Nocedal & Wright, 2006). Based on the approximation in Section 3.4.4, the primary thrust allocation problem can be formulated as follows:

$$\begin{aligned} J &= \min_{T_{th}} \{T_{th}^T W T_{th}\} \\ \text{subject to} \quad & T_a T_{th} = \tau_c \\ & A\, T_{th} \leq b \end{aligned} \tag{3.24}$$

Eq. 3.24 is the simplest form of the thrust allocation QP model. The inequality $A\, T_{th} \leq b$ represents the maximum and minimum thrust constraints discussed in Eq. 3.7 and Eq. 3.14. Fossen (2011) introduced a QP relaxed model with minimized power consumption and

largest thrust force. This relaxed model is adopted in this study as follows:

$$
\begin{aligned}
J = \min_{T_{th},s,f} \{ & T_{th}^T W T_{th} + s^T Q s + \beta \bar{f} \} \qquad (3.25) \\
\text{subject to} \quad & T_a T_{th} = \tau_c + s \\
& A\, T_{th} \leq b \\
& -\infty \leq s \leq \infty \\
& -\bar{f} \leq T_{th}(k) \leq \bar{f} \qquad (k = 1, 2, \cdots, 2n)
\end{aligned}
$$

where n is the number of thrusters; $s \in \mathbb{R}^3$ is a vector of slack variables; $Q \in \mathbb{R}^{3\times 3} \gg W > 0$ is the weighting matrix for s so that the slack variables will be close to zero; $\bar{f}$ is the largest thrust value in the vector T_{th} and $\beta \geq 0$ is used to weight $\bar{f}$.

In order to employ numerical QP solvers, Eq. 3.25 needs to be formulated in the standard QP form as the follows:

$$
\begin{aligned}
J = \min_{T_{th},s,f} & \begin{bmatrix} T_{th} \\ s \\ \bar{f} \end{bmatrix}^T \begin{bmatrix} W & 0 & 0 \\ 0 & Q & 0 \\ 0 & 0 & 0 \end{bmatrix} \begin{bmatrix} T_{th} \\ s \\ \bar{f} \end{bmatrix} + \begin{bmatrix} 0 \\ 0 \\ \beta \end{bmatrix}^T \begin{bmatrix} T_{th} \\ s \\ \bar{f} \end{bmatrix} \qquad (3.26) \\
\text{subject to} \quad & \begin{bmatrix} T_a & -I & 0 \end{bmatrix} \begin{bmatrix} T_{th} \\ s \\ \bar{f} \end{bmatrix} = \tau_c \\
& \begin{bmatrix} A & 0 & 0 \\ -I & 0 & -1 \\ I & 0 & -1 \end{bmatrix} \begin{bmatrix} T_{th} \\ s \\ \bar{f} \end{bmatrix} \leq \begin{bmatrix} b \\ 0 \\ 0 \end{bmatrix} \\
& \begin{bmatrix} -\infty \\ -\infty \end{bmatrix} \leq \begin{bmatrix} s \\ \bar{f} \end{bmatrix} \leq \begin{bmatrix} \infty \\ \infty \end{bmatrix}
\end{aligned}
$$

where I is the identity matrix. The matrix $\begin{bmatrix} T_{th} & s & \bar{f} \end{bmatrix}^T$ can be numerically obtained by QP

solvers.

In this study, a Fortran 77 package, "QuadProg" (Turlach, 1998), is integrated into the DEM program to solve the QP problem in Eq. 3.26. QuadProg is an open-source software for convex QP based on dual active-set method in Goldfarb and Idnani (1982, 1983). After Eq. 3.26 is solved by QuadProg, the thrust demand vector T_{th}, which contains the thrust value of each actuator in x and y axes, can be obtained.

Chapter 4

Results and Comparisons

4.1 Boom Towed in Tank

First, the numerical simulations were conducted to calculate the forces exerted on a boom when it was towed through a scaled broken ice field. The simulation domain dimensions are listed in Table 4.1. The values of ice rheology coefficients used in this case study are listed in Table 4.2. The simulation results were compared with results from Løset (1994b) in Table 4.3. Fig. 4.1 gives the comparison of the ice field snapshots of Run 1.1 at different instants.

Table 4.1: Simulation domain dimensions

Parameter	Unit	Value
Domain length	m	14
Domain width	m	7
Boom length	m	3
Ice disk radius	m	[0.15,0.20]

Compared with Løset (1994b), the ice fields have similar patterns. The error percentage in resistance predictions is small except for Run 1.2, where the boom is towed at doubled

Table 4.2: Values of ice rhelogy coefficients

Coefficient	Unit	Value
k_{ne}	N/m^2	1600
k_{te}	N/m^2	600
d_{nv}	$N{\cdot}s/m^2$	200

Table 4.3: Simulation setup, results and comparison

Run	Concentration	Ice Thickness (m)	Boom Speed (m/s)
1.1	60%	0.02	0.04
1.2	60%	0.02	0.08
1.3	40%	0.02	0.04
1.4	60%	0.04	0.04
1.5	70%	0.02	0.04
Run	Force per unit boom length (N/m)		
	Simulated	Løset (1994b)	Error Percentage
1.1	0.583	0.57	2.281%
1.2	1.369	1.9	27.94%
1.3	0.239	0.23	3.913%
1.4	1.166	1.16	5.172%
1.5	1.150	1.34	14.18%

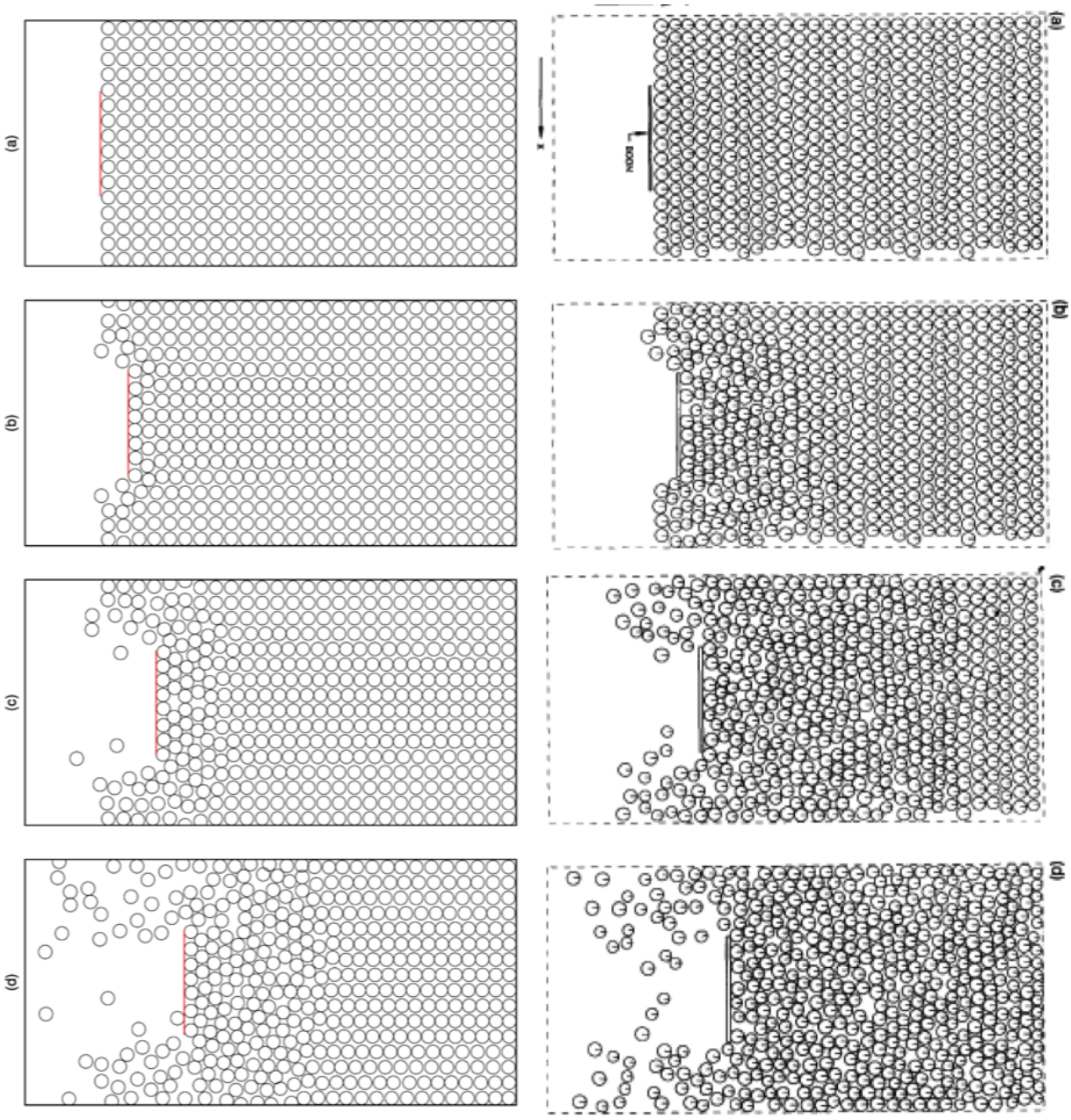

Figure 4.1: Field snapshots of Run 1.1g at (a) 0s, (b) 20s, (c) 40s, (d) 60s (Left: this study; Right: Løset(1994b))

speed. More than 10% error is found for Run 1.5, where the ice concentration is increased to 70%. The inaccuracy of Run 1.2 and Run 1.5 may be due to the effect of domain boundaries. Either high speed or greater ice concentration will cause more energetic interaction. Besides, the ice disks will interact with boundaries more often when the boom is in high speed, as the boom will reach closer to the other end of the domain.

4.2 R-Class Icebreaker Model Test

Simulations were also extended to a R-class icebreaker in a pack ice field. The results were compared to the model test data in Aboulazm (1989). The waterplane profile is presented in Fig. 4.2. The principal dimensions and parameters are listed in Table 4.4. The values of ice rheology coefficients used in this case study are listed in Table 4.5.

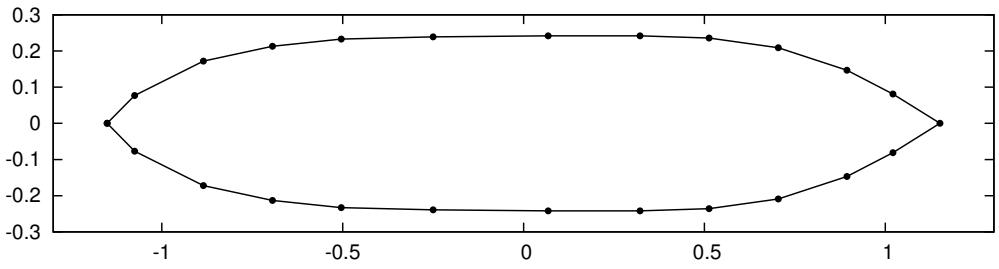

Figure 4.2: R-class model waterplane profile

The ship resistance was predicted numerically under different combinations of ship speed and ice conditions. Two sizes of triangle ice floes were used in the model tests. The areas of large and small ice floes are 0.032 m^2 and 0.016 m^2, respectively. As the numerical code was developed based on a circular particle geometry, the circumcircles of the triangles in two sizes were used for ice floe size in the simulation. The thickness of the ice floes were 0.0375 m.

Detailed setup information and results are presented in Table 4.6. The predicted ship resistance was averaged from the start when the ship was completely inside the pack ice field to the end of simulation. Snapshots of Run 2.3 at time of 0s, 10s, 20s are presented in Fig. 4.3. The time series of ship resistance for Run 2.3 are presented in Fig. 4.4.

Table 4.4: Icebreaker dimensions and parameters

Parameter	Unit	Value
Length water line	m	2.3
Draft	m	0.175
Beam	m	0.48
Mass	kg	120.625
Block Coefficient		0.624
Wet surface	m^2	1.1568

Table 4.5: Values of ice rhelogy coefficients

Coefficient	Unit	Value
k_{ne}	N/m^2	1200
k_{te}	N/m^2	450
d_{nv}	$N{\cdot}s/m^2$	70

Fig. 4.5 and 4.6 present the comparison of results between the model test and the numerical simulation for small and large ice floes, respectively. The large ice floe case shows a good agreement between experimental and numerical results when the ship speed increases. For the small ice floe case, a good agreement is obtained in low and medium ship speeds, but there is a slight discrepancy in high speed cases. In both figures, the tendency of resistance increasing is consistent between numerical and experimental results.

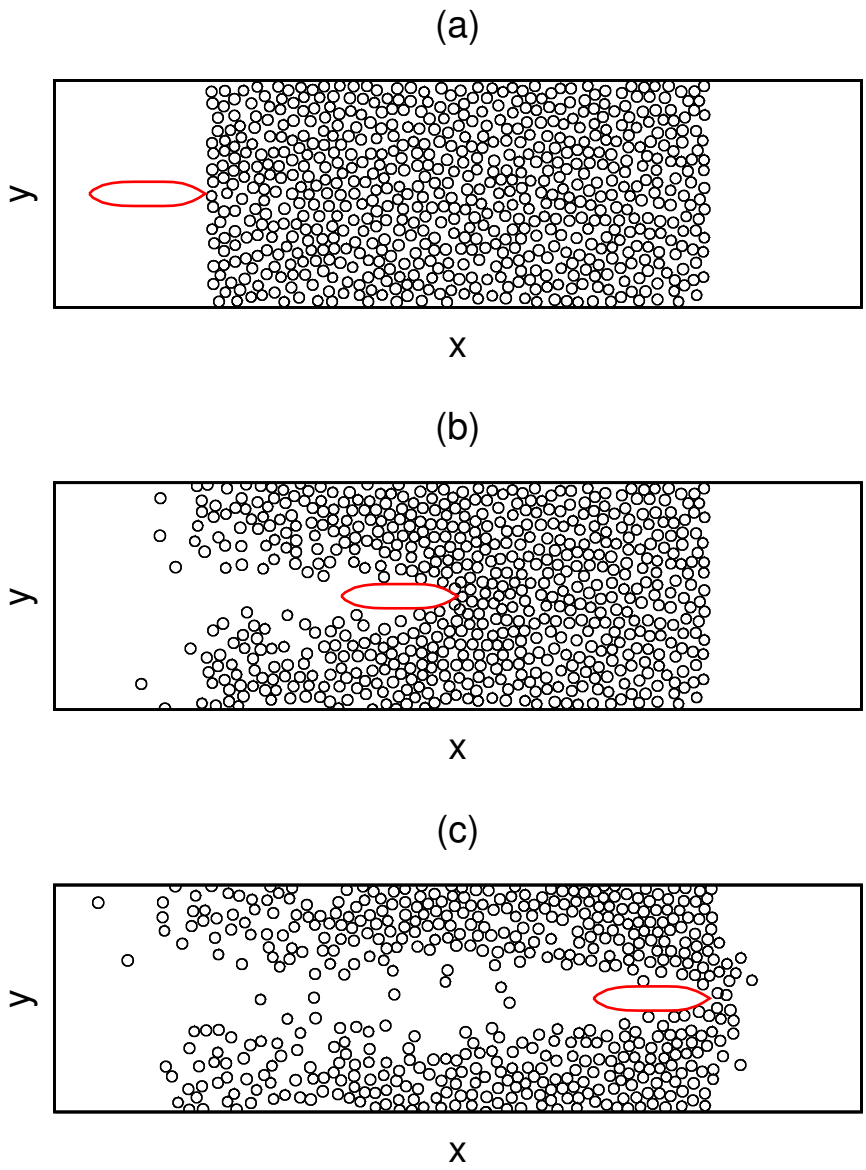

Figure 4.3: Field snapshots of a typical run at (a) 0s, (b) 10s, (c) 20s

Table 4.6: Simulation setup and results

Run	Floe Size	Concentration	Speed (m/s)	Simulated Resistance (N)
2.1	S	50%	0.3	1.564
2.2	S	50%	0.4	2.583
2.3	S	50%	0.5	3.923
2.4	S	50%	0.6	5.35
2.5	S	50%	0.7	7.415
2.6	S	50%	0.8	9.497
2.7	S	50%	0.9	11.598
2.8	S	50%	1	12.881
3.1	L	50%	0.3	2.092
3.2	L	50%	0.4	2.79
3.3	L	50%	0.5	4.707
3.4	L	50%	0.6	5.566
3.5	L	50%	0.7	6.585
3.6	L	50%	0.8	9.173
3.7	L	50%	0.9	11.141
3.8	L	50%	1	12.775

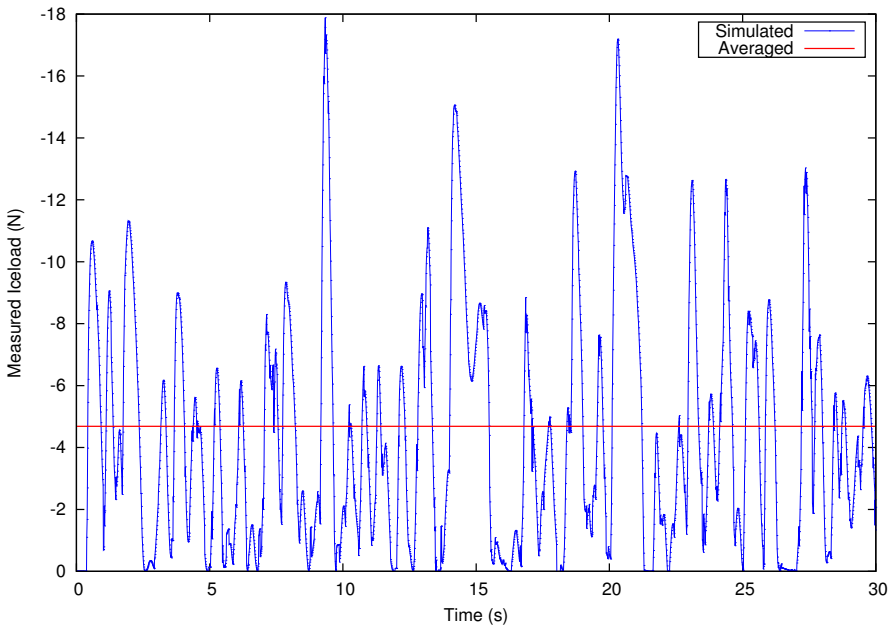

Figure 4.4: Ice-induced resistance time series of Run 3.3

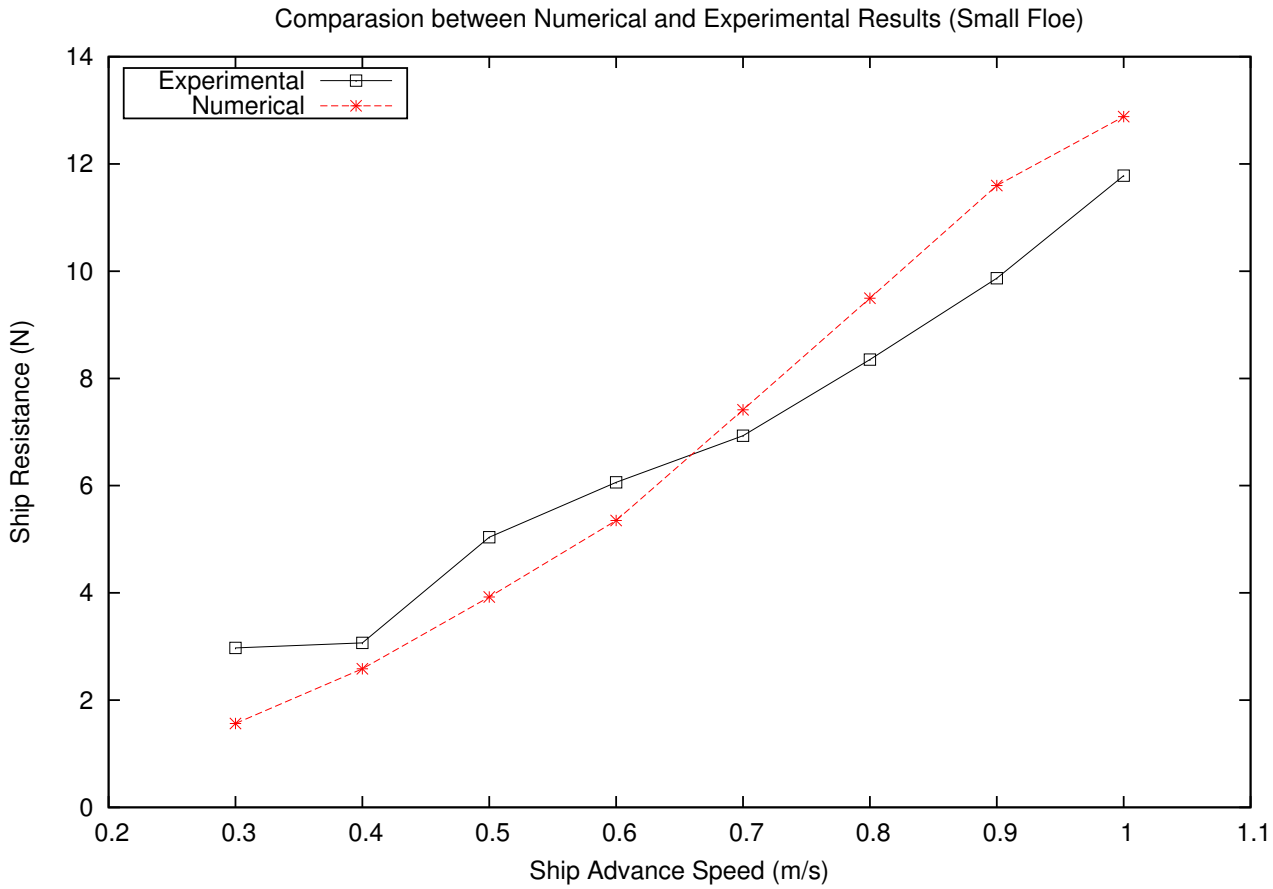

Figure 4.5: Validation with model test for Run 2.1 - 2.8

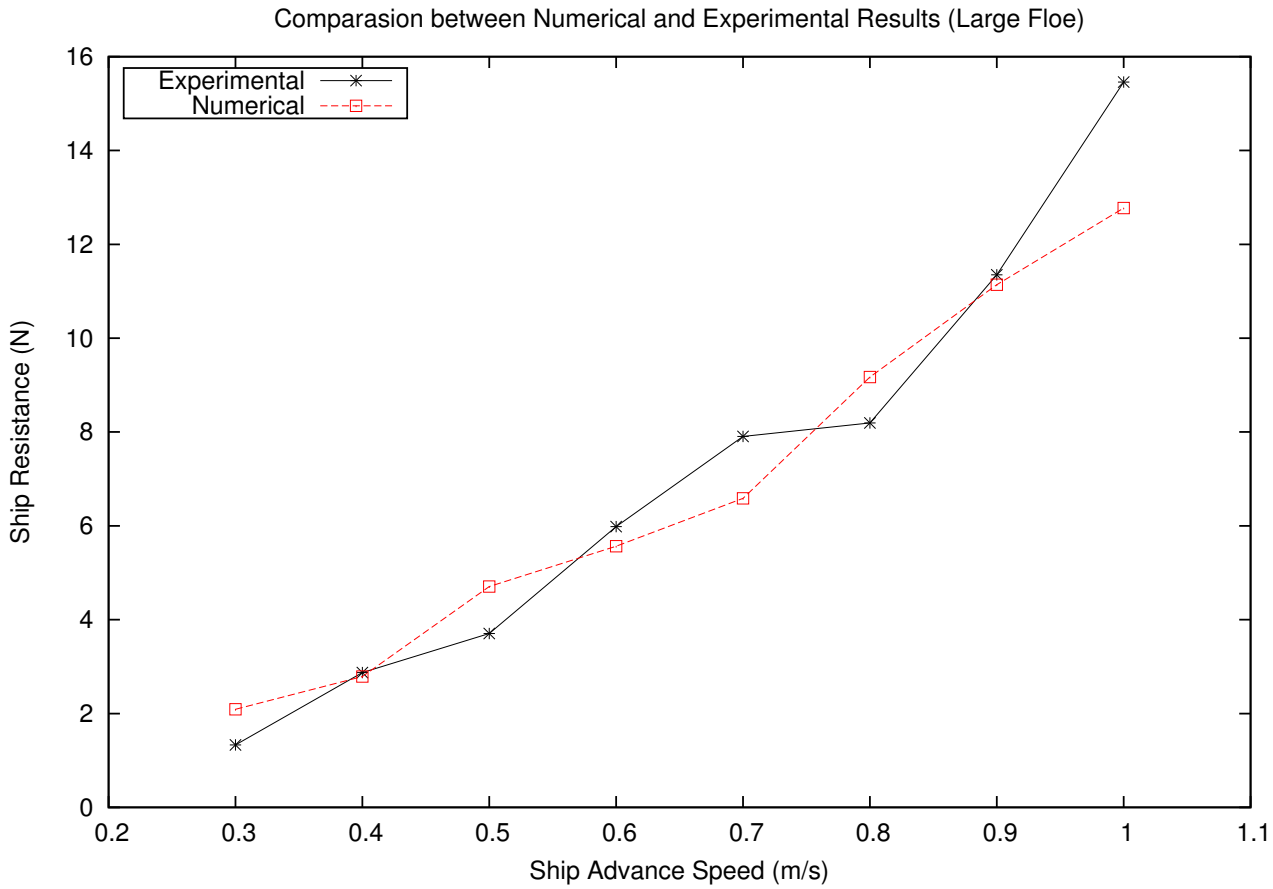

Figure 4.6: Validation with model test for Run 3.1 - 3.8

4.3 Arctic DP Vessel Case Studies

A series of full-scale numerical simulations were conducted with a sample arctic DP vessel. The vessel has two tunnel thrusters and two azimuth thrusters at bow, along with two azimuth thrusters at stern. The maximum power is 5 MW each for the two stern thrusters, and 1.5 MW each for the four thrusters at bow. The vessel sketch is shown in Fig. 4.7. The principle dimensions of the vessel and the thruster arrangements are listed in Table 4.7 and Table 4.8, respectively.

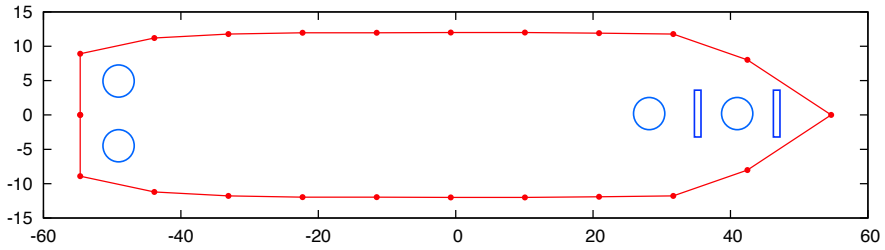

Figure 4.7: Sample arctic vessel waterplane sketch (Unit: m)

Table 4.7: Ship dimensions and parameters

Parameter	Notation	Value	Unit
Overall length	LOA	121.8	m
Length between perpendiculars	LPP	109.3	m
Beam	B	24.0	m
Depth of main desk	D	10.5	m
Design draft	T	6.5	m

Table 4.8: Thrusters arrangement in o-xyz frame

Thruster No.	Type	x-position	y-position
1	Tunnel	49.9	0
2	Azimuth	45.9	0
3	Tunnel	42.3	0
4	Azimuth	38.3	0
5	Azimuth	-52.5	-6
6	Azimuth	-52.5	6

4.3.1 PID Controller Performance Analysis

A series of simulations were conducted in open water to analyze the performance of the PID controller. As listed in Table 4.9, three sets of PID gains were used for the controller. Set 1 and Set 2 are used for position control, and Set 3 is used for heading control. When the distance between the ship's current location and the set-point location is larger than the ship length, Set 1 is used; otherwise, Set 2 is used.

Table 4.9: Values of PID gains

Set No.	K_p	K_i	K_d
1	2×10^5	0.05	1×10^4
2	1.5×10^4	0.05	6×10^4
3	9×10^7	1000	1.2×10^7

Table 4.10: Simulation PID settings

Run	Control setting
1	Only P control
2	PD control
3	PID control

The simulation domain is $400\,\mathrm{m} \times 400\,\mathrm{m}$. The initial status of the ship is static at $(300, 300)$ with 0° heading , and the set-point is at $(200, 200)$ with 0° heading. The wind and current both comes from 225° at speed of 0.5 m/s. Three simulations were conducted with different

PID control settings as listed in Table 4.10. The time series of the ship position simulated under the three controller settings are plotted in Fig. 4.8, Fig. 4.9 and Fig. 4.10, respectively.

It can be seen from the comparison between Fig. 4.8 and Fig. 4.9 that, the employment of the derivative gain significantly reduces the settling time and improves the stability of the system. Moreover, the comparison between Fig. 4.9 and Fig. 4.10 shows that the integral gain helps the system eliminate the steady-state error in Fig. 4.9.

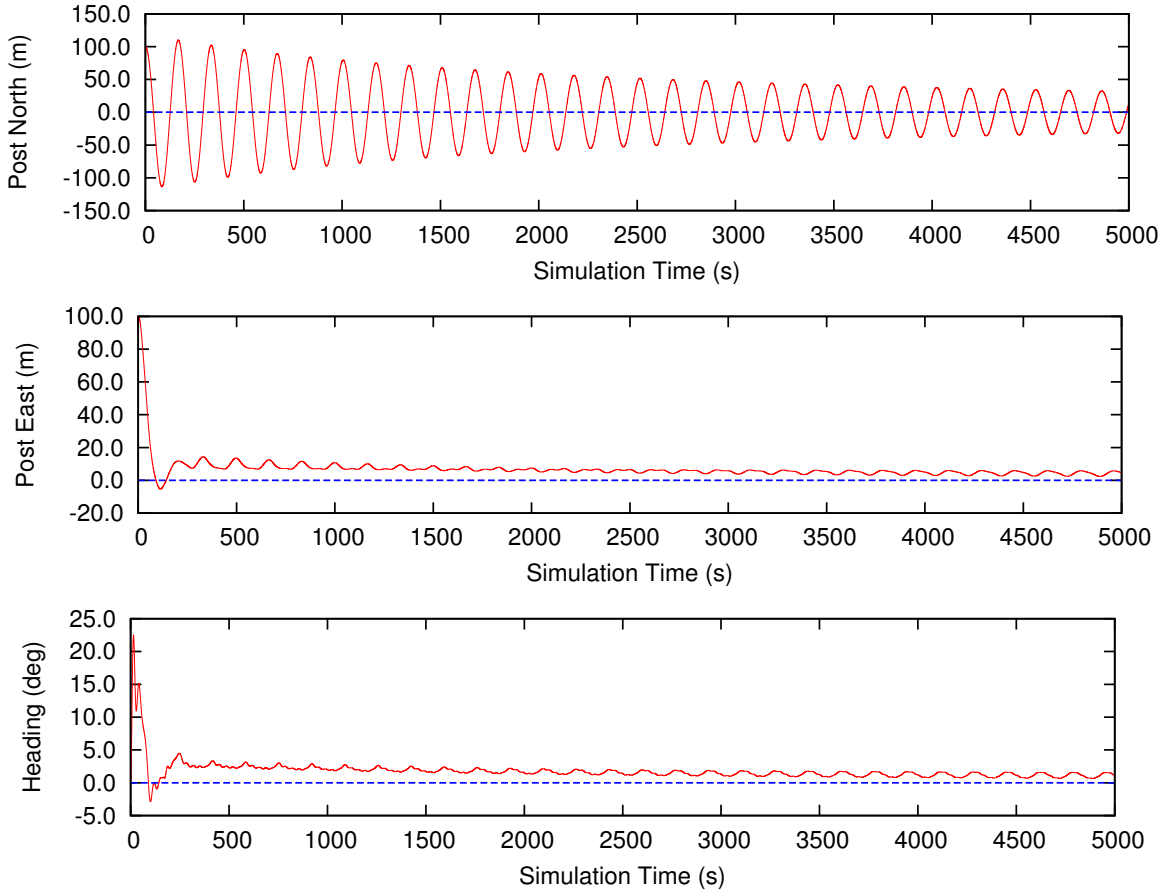

Figure 4.8: Time series of ship position and heading (Only P control)

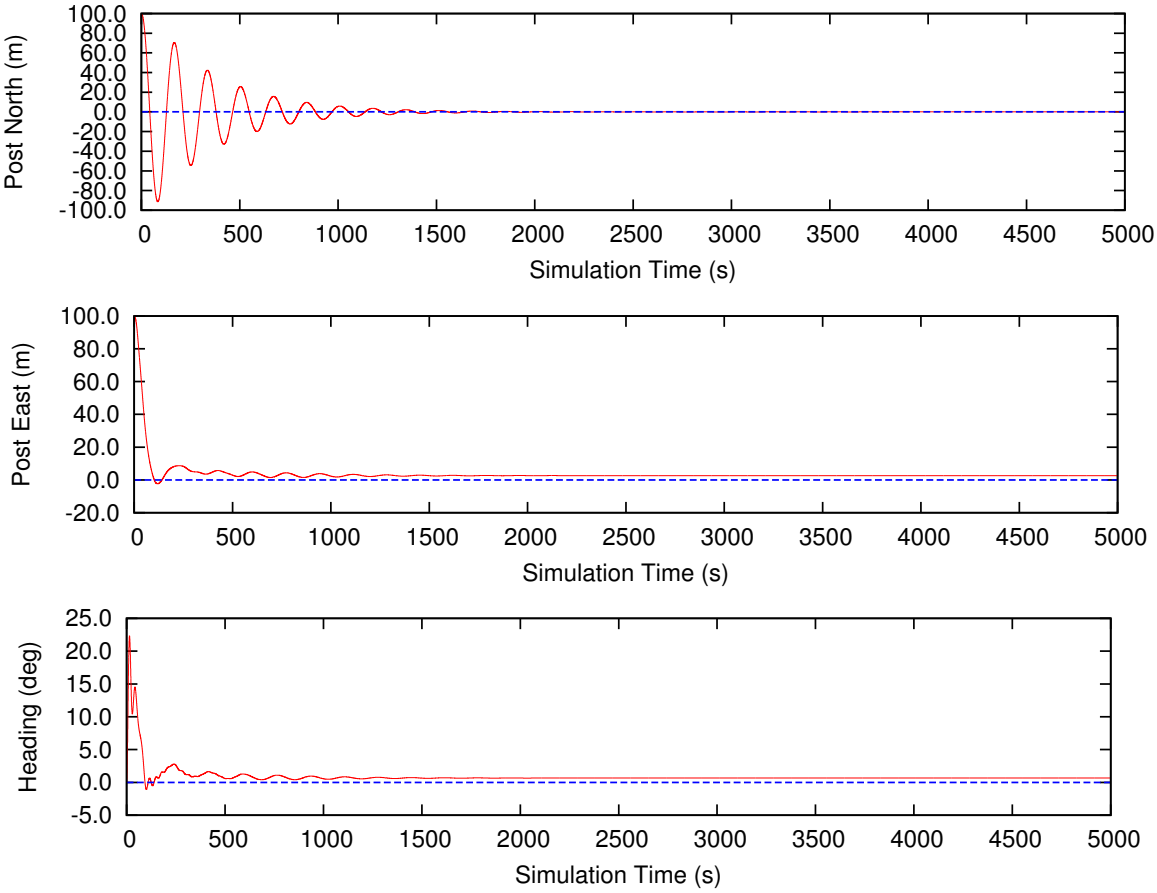

Figure 4.9: Time series of ship position and heading (PD control)

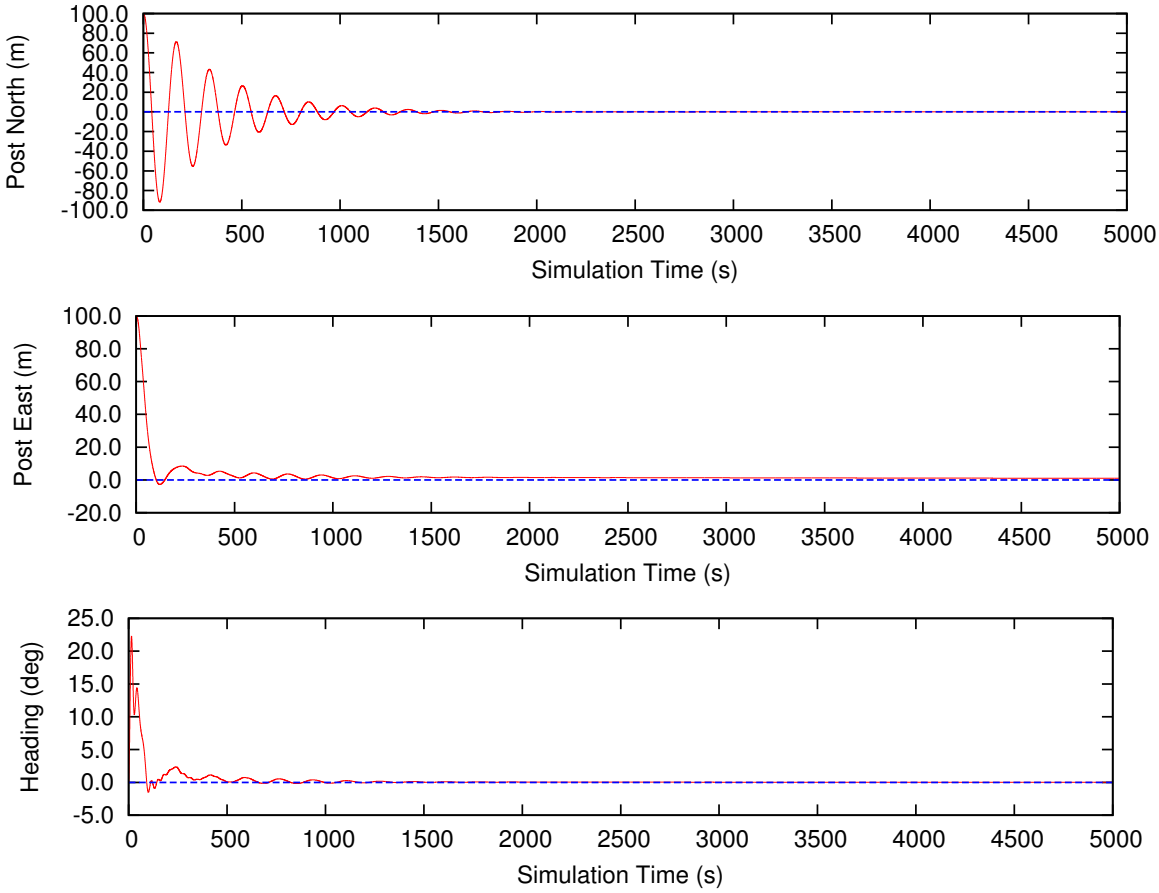

Figure 4.10: Time series of ship position and heading (PID control)

4.3.2 Arctic DP Capability Study

To study the DP performance in ice, a series of simulations were conducted in a 400 m×400 m pack ice field with 50% concentration. The field boundaries were set as periodic, which means when ice floes move beyond the boundary, they will be re-introduced from the other side of the boundary. The set-point for simulations was at $(200, 200)$ with 0° heading, and vessel initial position and heading were set to be same as the set-point. For simplicity and simulation computation speed, the ice floes were set to be in circular shape and thickness of 0.75 m. Ice floes were randomly distributed over the simulation domain and had radius ranging from 5 m to 10 m. The initial ice drift speed was set to be same as the current speed, which was 1 knot.

For DP operations in ice covered water, ice load is dominant compared to wind, wave and current loads. Therefore, the performance of the DP vessel is mainly impacted by the ice load. For simplicity, wind and current speeds were set to be constant and in same direction, and wave effects were neglected. The wind and current speeds were set as 3 knot and 1 knot, respectively. Table 4.11 is a summary of simulation conditions. The values of ice rheology coefficients used in this case study are listed in Table 4.12.

Simulation results with two current angles, 0° and 45°, were presented in this paper. Simulation snapshots with 0° current at selected instants are presented in Fig. 4.11. Fig. 4.12 presents the ship trajectories of both cases. Fig. 4.13 and Fig. 4.14 are the time series of ship 3 DOFs' motion and control force with 0 ° ice drift angle. Fig. 4.15 and Fig. 4.16 are the time series of ship 3 DOFs' motion and control force with 45 ° ice drift angle.

Table 4.11: Summary of simulation setups

Parameter	Value	Unit
Domain length	400	m
Domain width	400	m
Ice floe radius	[5,10]	m
Ice floe thickness	0.75	m
Ice concentration	50%	
Initial ice drift speed	1	knot
Wind speed	3	knot
Current speed	1	knot
Vessel initial position	(200,200)	m
Vessel initial heading	0	deg
Vessel desired position	(200,200)	m
Vessel desired heading	0	deg
Vessel initial velocity (u, v, r)	$(0, 0, 0)$	$(\mathrm{m/s}, \mathrm{m/s}, \mathrm{rad/s})$

Table 4.12: Values of ice rhelogy coefficients

Coefficient	Unit	Value
k_{ne}	$\mathrm{N/m^2}$	2×10^6
k_{te}	$\mathrm{N/m^2}$	6×10^5
d_{nv}	$\mathrm{N{\cdot}s/m^2}$	2×10^5

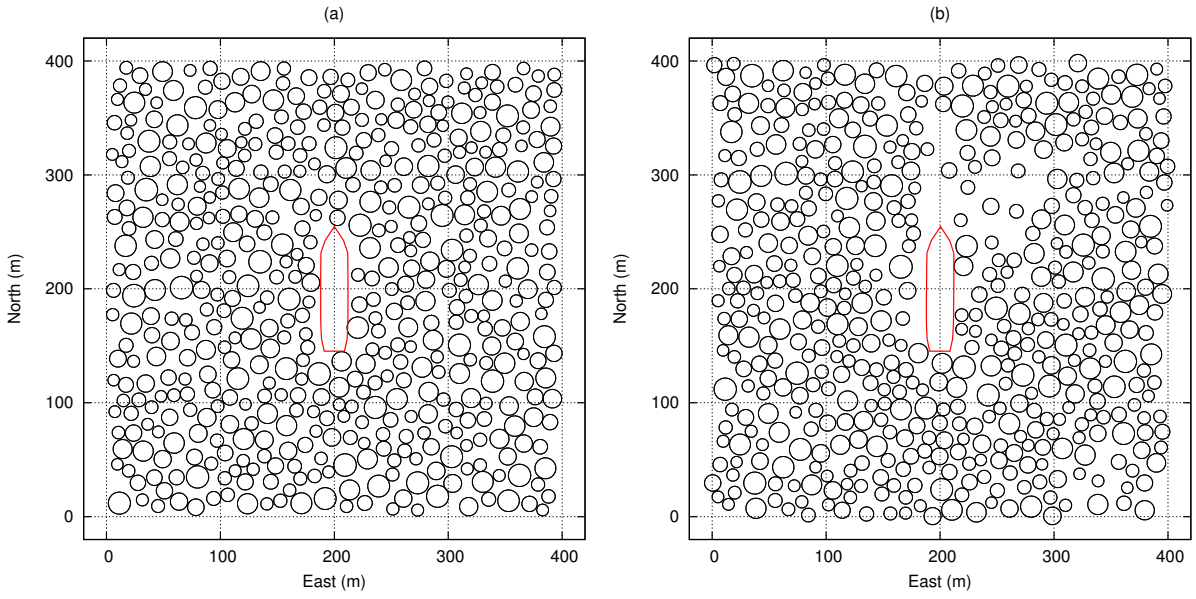

Figure 4.11: Simulation domain snapshots at (a) 0s; (b) 200s

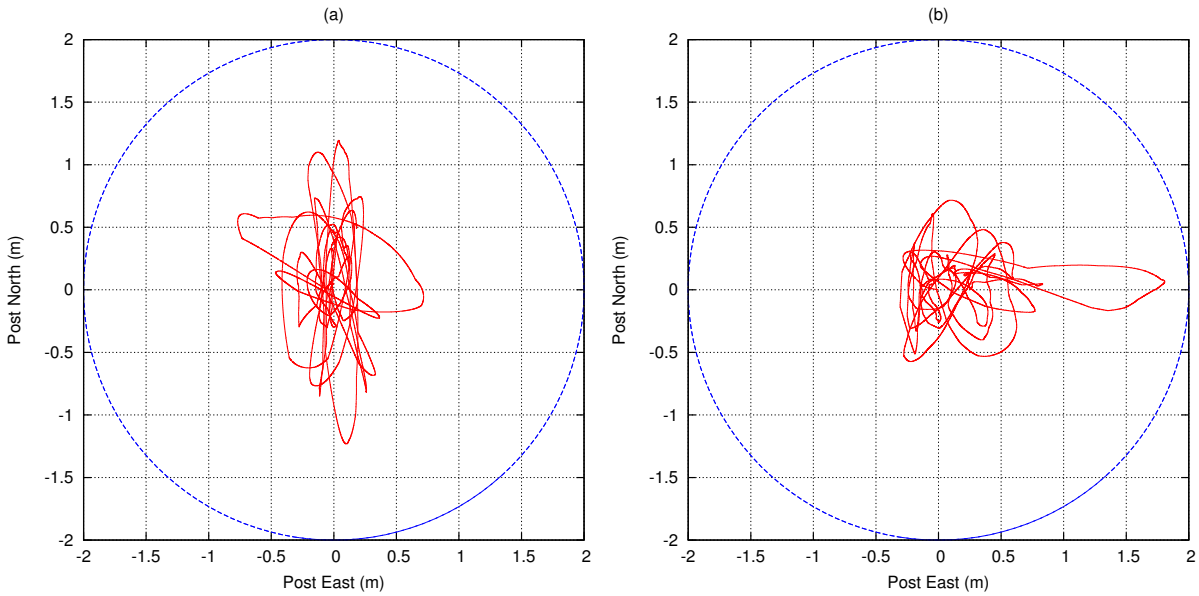

Figure 4.12: Ship trajectory (ice drift angle= (a) 0°; (b) 45°)

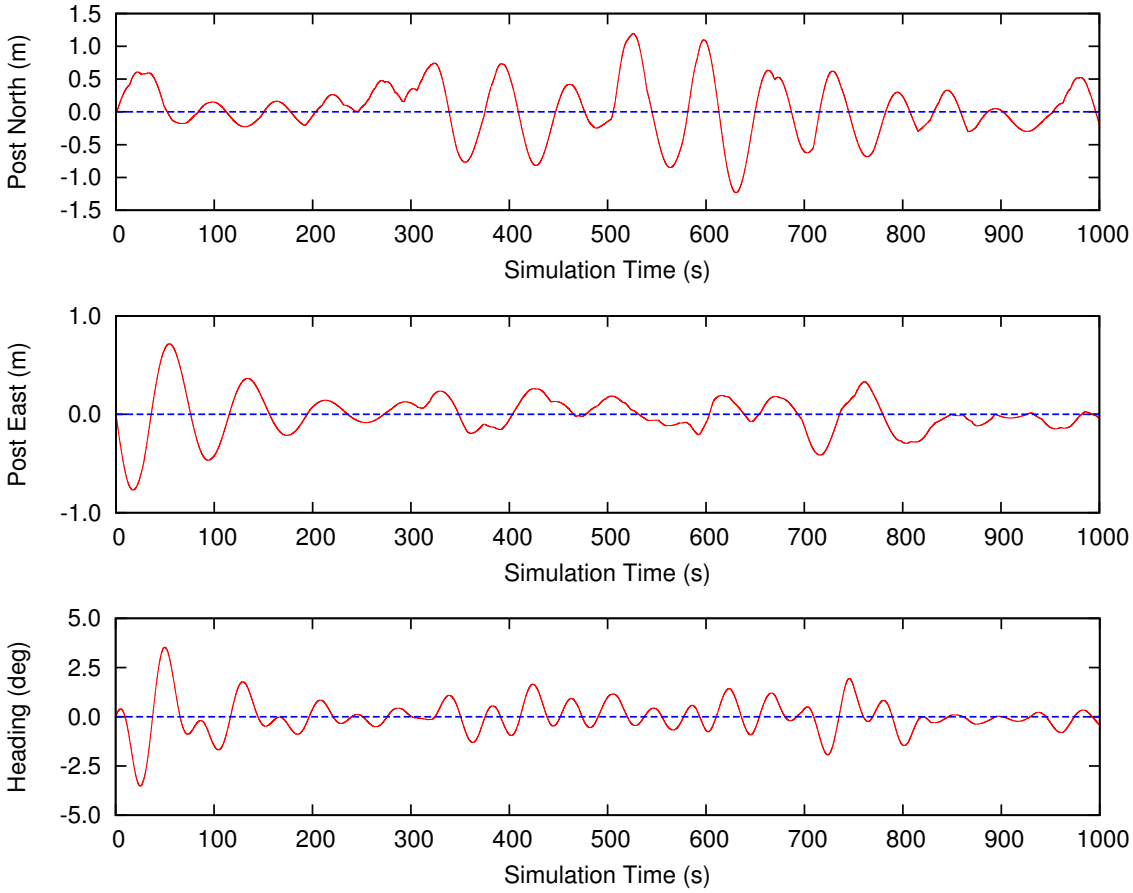

Figure 4.13: Time series of ship position and heading (ice drift angle=0°)

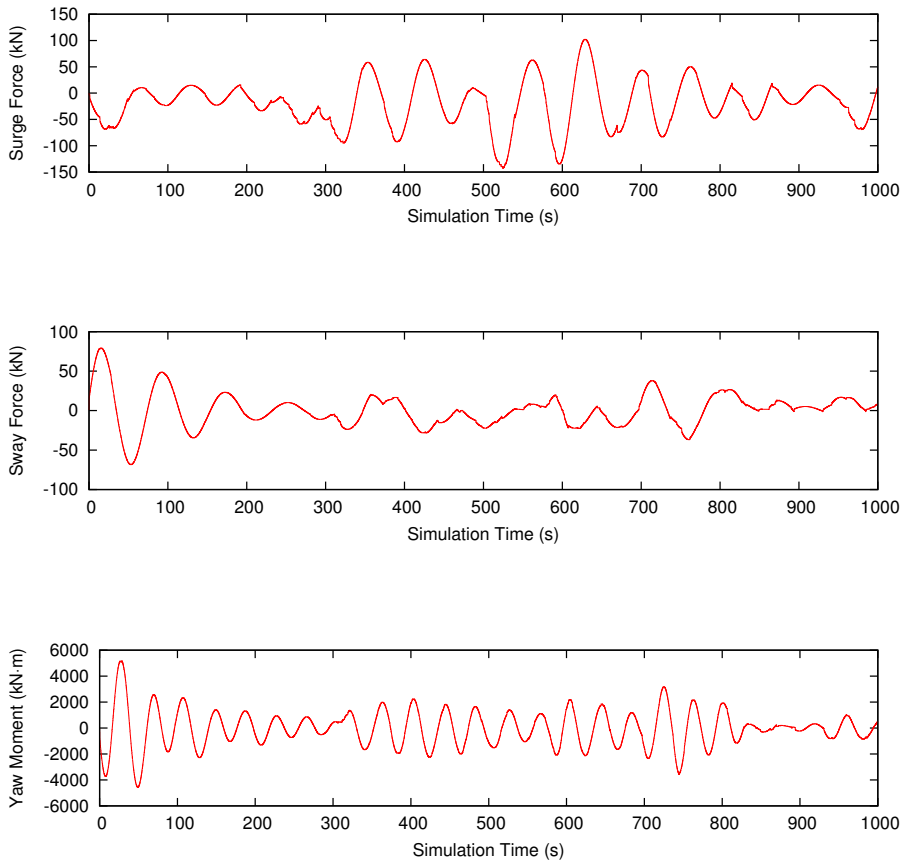

Figure 4.14: Time series of control force and moment in (a) surge; (b) sway; (c) yaw (ice drift angle=0°)

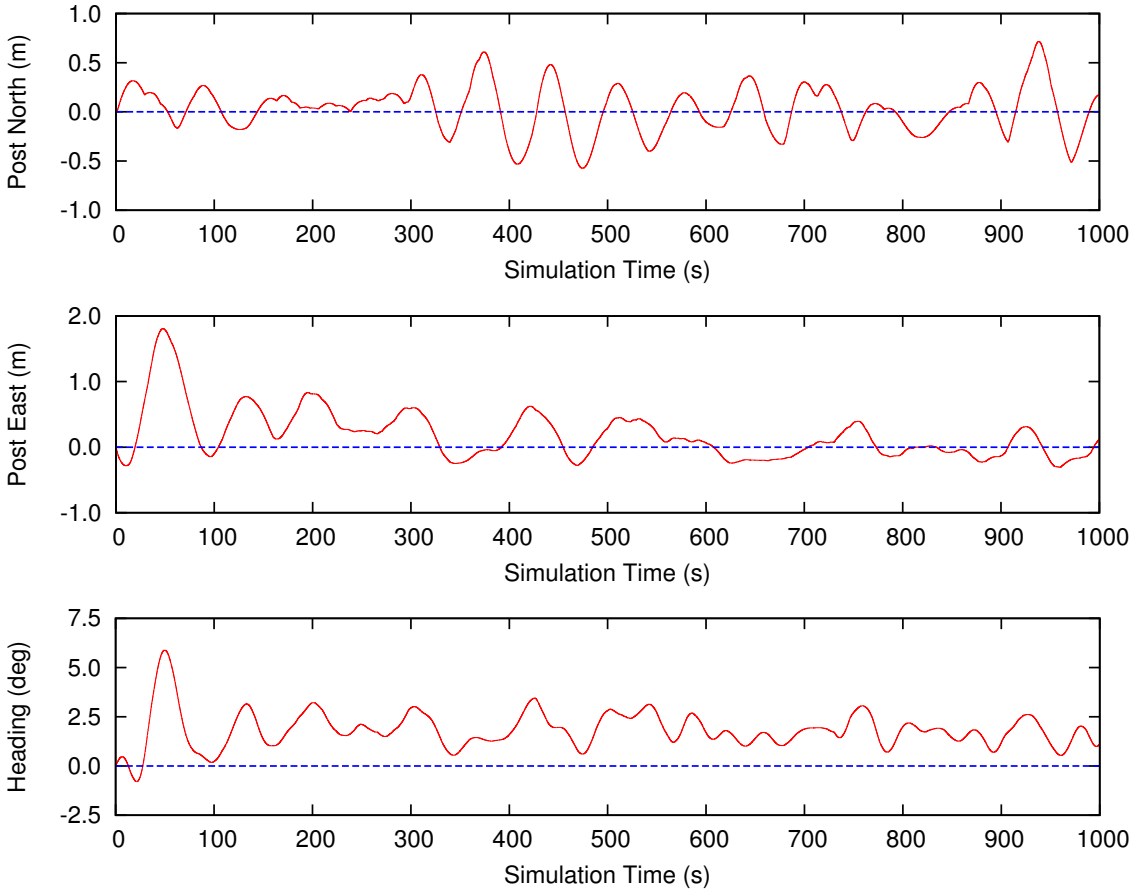

Figure 4.15: Time series of ship position and heading (ice drift angle=45°)

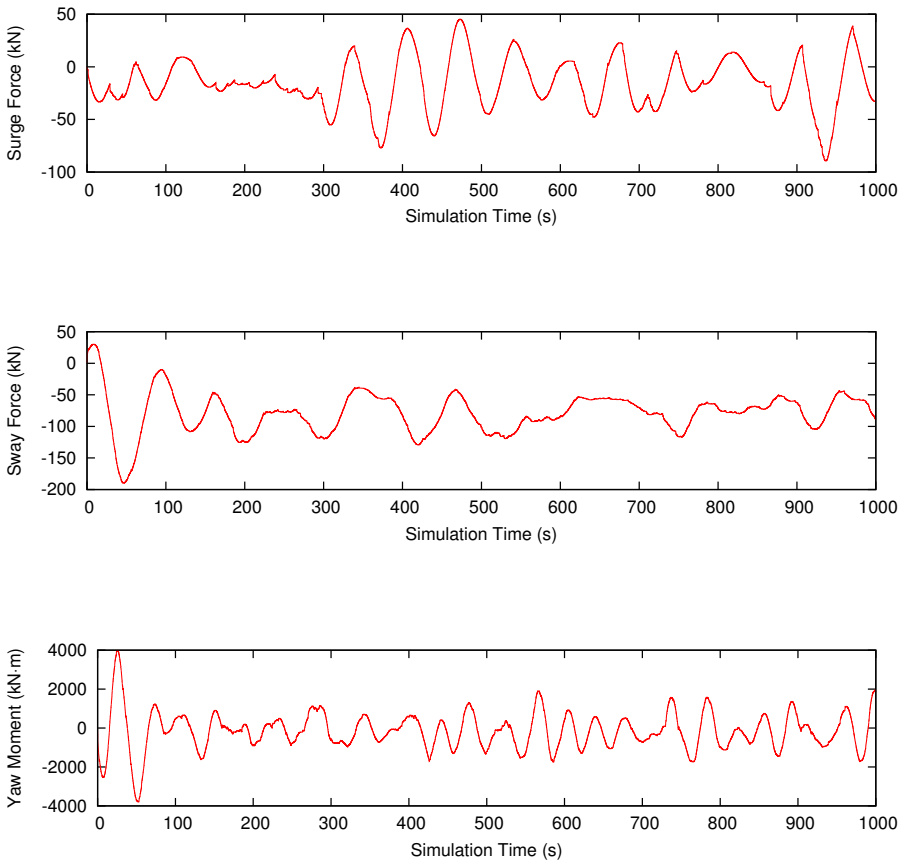

Figure 4.16: Time series of control force and moment in (a) surge; (b) sway; (c) yaw (ice drift angle=45°)

It can be seen from Fig. 4.12 that the ship's positions were well kept within a watch circle with radius 2 m for both ice drift angles. When ice drift angle is 45 °, the ship experienced a relatively large deviation towards the East in the beginning of the simulation, but later on the ship was controlled within a close distance to the set-point. The relatively large deviation was due to low control forces and large discrete ship-ice interaction force in the beginning of the simulation. Moreover, the ship control ability was weaker in sway and yaw than surge, especially for yaw control as huge yaw moments will come from ice loads in transversal direction. Fig. 4.17 is the vessel's DP capability plot, where the radical coordinate is the ice drift speed in m/s and the angular coordinate is the angle that the ice floes come from. The black line indicates the DP capability when the thrust system is intact, while the red one indicates the DP capability when the azimuth thruster No. 6, fails. The DP capability is good at head and following sea, and evident decrease can be found at beam sea or thruster failure cases.

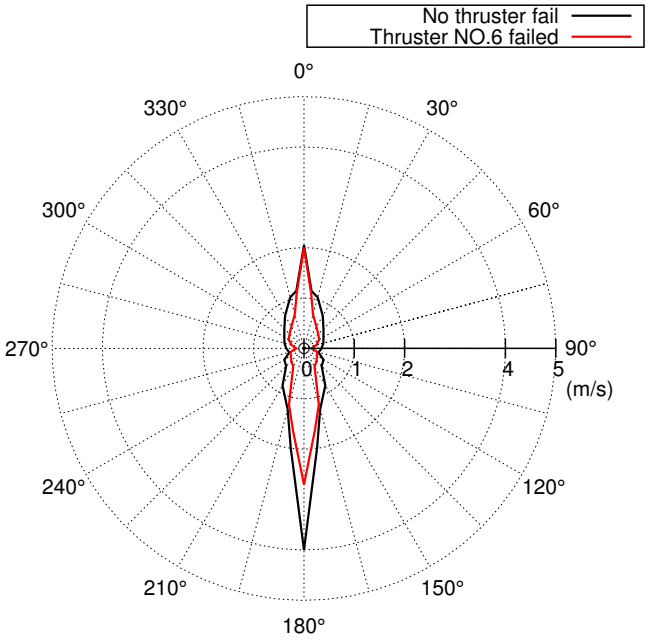

Figure 4.17: DP capability plot

Chapter 5

Conclusions and Recommendations

5.1 Conclusions

This study is set out to find a numerical approach to effectively simulate DP operations in pack ice fields. The reasons and motivation for this study is the increasing importance of the Arctic resources and the advantage of DP systems. In this thesis, a discrete element method is adopted to calculate the interaction forces and a DP control system with a thrust allocator is developed.

The main contributions of the thesis are summarized as below:

- A literature review of pack ice load calculation and DP simulation in pack ice is provided. The review covers the major empirical and analytical works. It also includes different types of numerical models and experiment studies in full scale and model scale. One notable fact is that the DEM models have been increasing popular in this area and a variety of DEM studies have been proposed by researchers all over the world. Unfortunately, the major effort in the Arctic research area was focused on level ice in the past few decades, and the resources in the public domain are limited, therefore, this review may not be thorough.

- A 3 DOF time-domain numerical model is developed based on DEM. In this model, a viscous-elastic ice rheology is adopted to simplify and predict the complicated ice interaction forces.
- A DP control system is built to fulfill stationkeeping in pack ice. In this control system, a PID controller is coupled with a constrained thrust allocation algorithm which is developed with quadratic programming.
- The DEM numerical model is verified and validated with former researchers' simulations and model tests. The feasibility and capability of the DP control system is researched by simulating a sample Arctic vessel.

Based on the simulation results and comparisons, the following conclusions can be drawn:

- The real ship-ice or ice-ice collision is a highly non-linear and stiff process. However, with a certain level of linearization, a soft-particle approach can simulate and predict the macro-level loads of the process.
- The ship resistance in pack ice field is proportional to ship speed and ice thickness.
- The ship-ice interaction force increases as the ice concentration or the ice floe size increases, but the relationship is not linear.
- The ice loads are dominant to ship dynamics. A realistic ship-ice interaction prediction can certainly improve the performance of the DP system.
- The ship control ability in yaw motion is weaker than surge and sway. When ice drift angle is large, the ship will probably struggle with yaw control and experience deviation from set-point.

5.2 Recommendations and Future Work

The ultimate scope of this study is to develop a software with versatility of simulating different ship operations in various ice conditions. This study also sought to effective and

relatively accurate solutions to ship-ice interaction problems, so that this study can provide assistance or reference for other researchers dealing with ice-related works. This thesis, as a preliminary work of the whole scope, contains simplified numerical model and specified ice conditions with assumptions to the environment complexity. The effort of future works can be made to the following aspects:

- The ice floes used in this study are circular-shaped because of the limitation of interaction detection algorithm. It would be realistic and necessary to have random shaped polygon floe in the future. In order to have this feature, the ice generating algorithm and the current collision algorithm regarding the geometry should be updated accordingly.

- Another issue about the floe shape is the ice concentration. With circular-shaped ice floes, the maximum ice concentration can be achieved is approximately 78%, which is fine with simulations of brash ice and managed broken ice fields. However, it would be interesting to explore the software's performance in high-concentrated ice fields, especially comparing to level ice when concentration is higher than 95%. On the other hand, in order to improve the software's versatility, high ice concentration is an important feature to have.

- The tangential friction effect can be significant in an ice-ice collision. A tangential friction force should be considered in the future.

- The current ship manoeuvring model is in 3 DOF, which neglected the roll, pitch and heave motions. And the ice force calculation is also limited in the horizontal plane. 6 DOF motion and force model should be considered in the future.

- For the control system, the current controller is a basic PID controller. More advanced controllers might be considered in the future. Moreover, Kalman filter would be a good feature to integrate, in order to get preciser measurement of the control signal.

- In the current model, the thrust forces are assumed to be applied on the vessel instantaneously. A more realistic thruster RPM model should be studied in the future.

References

Aboulazm, A. F. (1989). *Ship Resistance in Ice Floe Covered Waters*. Unpublished doctoral dissertation, Memorial University of Newfoundland.

Aboulazm, A. F., & Muggeridge, D. (1989). Analytical Investigation of Ship Resistance in Broken or Pack Ice. In *Proceedings of the Eighth International Conference on Offshore Mechanics and Arctic Engineering* (Vol. 4).

Alawneh, S., Dragt, R., Peters, D., Daley, C., & Bruneau, S. (2015). Hyper-Real-Time Ice Simulation and Modeling Using GPGPU. *IEEE Transactions On Computers*.

Alawneh, S., & Peters, D. (2012). Ice Simulation Using GPGPU. In *2012 IEEE 14th International Conference on High Performance Computing and Communication* (pp. 425–431).

Babić, M. (1988). *Discrete Particle Numerical Simulation of Granular Material Behavior* (Tech. Rep. No. 88-11). Department of Civil and Environmental Engineering, Clarkson University.

Balchen, J. G., Jenssen, N. A., & Sælid, S. (1976). Dynamic Positioning Using Kalman Filtering and Optimal Control Theory. In *IFAC/IFIP Symposium on Automation in Offshore Oil Field Operation* (Vol. 183, p. 186).

Barker, A., Sayed, M., & Timco, G. (2000a). *Numerical Simulations of Broken Ice Interaction with Structures* (Tech. Rep. No. HYD-TR-050). Canadian Hydraulics

Centre, National Research Council of Canada, Ottawa.

Barker, A., Sayed, M., & Timco, G. (2000b). Numerical Simulation of Floating Ice Forces on Bridge Piers. In *Proceedings of Annual Conference of the Canadian Society for Civil Engineering* (pp. 243–249).

Barker, A., & Timco, G. (2003). The Effect of Structure Shape on the Broken Ice Zone Surrounding Offshore Structures. In *Proceedings of the 17th International Conference on Port and Ocean Engineering under Arctic Conditions POAC'03* (Vol. 2, pp. 787–796).

Blanke, M., Kinnaert, M., Lunze, J., & Staroswiecki, M. (2003). *Diagnosis and Fault-Tolerant Control*. Springer.

Bronnikov, A. V. (1959). Analysis of Resistance of Cargo Ships Going Through Pack Ice. *Transactions of Leningrad Shipbuilding Institute*(27), 13.

Buzuev, A., & Ryvlin, A. (1961). Calculation of the Resistance Encountered by an Icebreaker Moving Through Ice Cakes and Brash. *Morskoi Flot*, *21*(8), 136–138.

Buzuev, A., & Ryvlin, A. (1966). Calculation of Ice Resistance to the Movement of an Icebreaker under Different Ice Conditions. *Problems of the Arctic and the Antarctic*.

Cammaert, A., & Muggeridge, D. (1988). *Ice Interaction with Offshore Structures*. Van Nostrand Reinhold Co. Inc., New York, NY.

Comfort, G., Singh, S., & Spencer, D. (1999). *Evaluation of Ice Model Test Data for Moored Structures* (Tech. Rep. No. 26-195). Ottawa, Canada: Canadian Hydraulics Centre, National Research Council of Canada.

Croasdale, K., Bruce, J., & Liferov, P. (2009). Sea Ice Loads due to Managed Ice. In *Proceedings of the International Conference on Port and Ocean Engineering Under Arctic Conditions.*

Cundall, P. A. (1971). A Computer Model for Simulating Progressive, Large-Scale

Movements in Blocky Rock Systems. In *Proceedings of the Symposium of the International Society for Rock Mechanics, Nancy, France* (Vol. 2(8), p. 129-136).

Cundall, P. A., & Strack, O. D. (1979). A Discrete Numerical Model for Granular Assemblies. *Geotechnique*, *29*(1), 47–65.

Daley, C. (1999). Energy Based Ice Collision Forces. In *Proceedings of the 15th International Conference on Port and Ocean Engineering under Arctic Conditions, Helsinki University of Technology in Espoo, Finland.*

Daley, C. (2014, February). GPU-Event-Mechanics Evaluation of Ice Impact Load Statistics. In *Arctic Technology Conference.* Houston, Texas, USA.

Daley, C., Alawneh, S., Peters, D., Quinton, B., & Colbourne, B. (2012). GPU Modeling of Ship Operations in Pack Ice. In *International Conference and Exhibition on Performance of Ships and Structures in Ice, Banff Alberta, Canada September* (pp. 20–23).

Dal Santo, X., & Jochmann, P. (2012). Model DP System for Ice-Tank Research. In *ASME 2012 31st International Conference on Ocean, Offshore and Arctic Engineering* (pp. 473–476).

De Wit, C. (2009). *Optimal Thrust Allocation Methods for Dynamic Positioning of Ships.* Unpublished doctoral dissertation, Delft University of Technology, Delft, the Netherlands.

Eskola, H. (1983). Propulsion Tests of a Ship Model in Conditions Simulating an Old Ice-Clogged Channel. In *Proceedings of the 7th International Conference on Port and Ocean Engineering under Arctic Conditions, Helsinki, Finland* (p. 494-506).

Ettema, R., Matsuishi, M., & Kitazawa, T. (1986). Model Tests on Ice-Rubble Size and Ship Resistance in Ice Rubble. *Cold Regions Science and Technology*, *12*(3), 229–243.

Flato, G. M. (1993). A Particle-in-Cell Sea-Ice Model. *Atmosphere-Ocean*, *31*(3), 339–358.

Fossen, T. I. (1994). *Guidance and Control of Ocean Vehicles*. Wiley New York.

Fossen, T. I. (2011). *Handbook of Marine Craft Hydrodynamics and Motion Control*. John Wiley & Sons.

German, J. G., Sterling, J., Benjamin, A., Timonen, P., & Hearnshow, J. D. (1981). Data Collection System on Board the Ice-Strengthened Cargo Vessel M.V. Arctic for Evaluation of Ship Performance in Ice. In *The Society of Naval Architects and Marine Engineers, Ice Tech Symposium, Ottawa, Canada.*

Gill, R., Aboulazm, A. F., Terry, B., & Russell, W. (1981). A Ship Transit Model for Passage through Ice and Its Application to the Labrador Area. In *The society of naval architects and marine engineers, sprint meeting, ottawa, canada.*

Goldfarb, D., & Idnani, A. (1982). Dual and Primal-Dual Methods for Solving Strictly Convex Quadratic Programs. In *Numerical analysis* (pp. 226–239). Springer.

Goldfarb, D., & Idnani, A. (1983). A Numerically Stable Dual Method for Solving Strictly Convex Quadratic Programs. *Mathematical Programming*, *27*(1), 1–33.

Gong, I.-Y. (1993). *Development of Maneuvering Simulation Program, Part I: Mathematical Models for Maneuvering Motions in Deep/Shallow Water with Wind/Current Effects* (Tech. Rep. No. IR-1993-09). Institute for Marine Dynamics, National Research Council Canada.

Greisman, P. (1981). *Brash Ice Behavior* (Tech. Rep. No. CGRDC-9/81). U.S. Coast Guard Research and Development Center, Groton, CN, USA.

Gutfraind, R., & Savage, S. B. (1998). Flow of Fractured Ice through Wedge-Shaped Channels: Smoothed Particle Hydrodynamics and Discrete-Element Simulations. *Mechanics of Materials*, *29*(1), 1-17.

Haase, A., & Jochmann, P. (2013). DYPIC-Dynamic Positioning in Ice: Second

Phase of Model Testing. In *ASME 2013 32nd International Conference on Ocean, Offshore and Arctic Engineering.*

Haase, A., van der Werff, S., & Jochmann, P. (2012). DYPIC-Dynamic Positioning in Ice: First Phase of Model Testing. In *ASME 2012 31st International Conference on Ocean, Offshore and Arctic Engineering* (pp. 487–494).

Hals, T., & Jenssen, N. A. (2012). DP Ice Model Test of Arctic Drillship and Polar Research Vessel. In *ASME 2012 31st International Conference on Ocean, Offshore and Arctic Engineering* (pp. 467–472).

Hansen, E. H., & Løset, S. (1999a). Modelling Floating Offshore Units Moored in Broken Ice: Model Description. *Cold Regions Science and Technology*, *29*(2), 97–106.

Hansen, E. H., & Løset, S. (1999b). Modelling Floating Offshore Units Moored in Broken Ice: Comparing Simulations with Ice Tank Tests. *Cold Regions Science and Technology*, *29*(2), 107–119.

Hespanha, J. P., & Morse, A. S. (2002). Switching between Stabilizing Controllers. *Automatica*, *38*(11), 1905–1917.

Hirano, M. (1981). A Practical Calculation Method of Ship Maneuvering Motion at Initial Design Stage. *Naval Architecture and Ocean Engineering*, *19*, 68–80.

Hocking, G., Mustoe, G., & Williams, J. (1987). Dynamic Analysis for Generalized Three Dimensional Contact and Fracturing of Multiple Bodies. In *Proceedings of the NUMETA 1987, Numerical Methods of Engineering, Theory and Applications.* Swansea, UK.

Holtrop, J. (1984). A Statistical Re-analysis of Resistance and Propulsion Data. *International Shipbuilding Progress*, *31*(363), 272–276.

Hopkins, M. A. (1992). *Numerical Simulation of Systems of Multitudinous Polygonal Blocks* (Tech. Rep. No. 92-22). U.S. Army CRREL.

Jenssen, N. A., Hals, T., Jochmann, P., Haase, A., dal Santo, X., Kerkeni, S., ... Løset, S. (2012). DYPIC–A Multi-National R&D Project on DP Technology in Ice. In *Proceedings of the Dynamic Positioning Conference 2012, Houston, Texas, USA*.

Jenssen, N. A., Muddesitti, S., Phillips, D., & Backstrom, K. (2009). DP in Ice Conditions. In *Dynamic Positioning Conference* (pp. 13–14).

Karulin, E. B., & Karulina, M. M. (2011). Numerical and Physical Simulations of Moored Tanker Behaviour. *Ships and Offshore Structures*, *6*(3), 179–184.

Kashteljan, V., Poznjak, I., & Ryvlin, A. (1969). *Ice Resistance to Motion of a Ship*. Marine Computer Application Corporation.

Keinonen, A., Browne, R., Revill, C., & Reynolds, A. (1996). *Icebreaker Characteristics Synthesis* (Tech. Rep. No. TP 12812E). Transportation Development Centre, Transport Canada, Calgary.

Keinonen, A., & Robbins, I. (1998). *Icebreaker Performance Models, Seakeeping, Icebreaker Escort, Vol. 3 – Icebreaker Escort Model User's Guide* (Tech. Rep.). Transport Canada, Calgary.

Keinonen, A., Shirley, M., Liljestrom, G., & Pilkington, R. (2006). Transit and Stationary Coring Operations in the Central Polar Pack. In *Proceedings of ICETECH.* Calgary, Canada.

Keinonen, A., Wells, H., Dunderdale, P., Pilkington, R., Miller, G., Brovin, A., et al. (2000). Dynamic Positioning Operation in Ice, Offshore Sakhalin, May-June 1999. In *Proceedings of the 10th International Offshore and Polar Engineering Conference.* Seattle, USA.

Kerkeni, S., Dal Santo, X., & Metrikin, I. (2013a). Dynamic Positioning in Ice: Comparison of Control Laws in Open Water and Ice. In *ASME 2013 32nd International Conference on Ocean, Offshore and Arctic Engineering.*

Kerkeni, S., Metrikin, I., & Jochmann, P. (2013b). Capability Plots of Dynamic Positioning in Ice. In *ASME 2013 32nd International Conference on Ocean, Offshore and Arctic Engineering.*

Kim, M.-C., Lee, S.-K., Lee, W.-J., & Wang, J.-y. (2013). Numerical and Experimental Investigation of the Resistance Performance of an Icebreaking Cargo Vessel in Pack Ice Conditions. *International Journal of Naval Architecture and Ocean Engineering*, *5*(1), 116-131.

Kitazawa, T., & Ettema, R. (1986). Rubble-Ice Resistance for Ships Moving with Creeping Speed. In *Proceedings of the 5th International Conference on Offshore Mechanics and Arctic Engineering, Tokyo.*

Kjerstad, Ø., Metrikin, I., Løset, S., & Skjetne, R. (2015). Experimental and Phenomenological Investigation of Dynamic Positioning in Managed Ice. *Cold Regions Science and Technology*, *111*, 67-79.

Kjerstad, Ø., & Skjetne, R. (2014). Modeling and Control for Dynamic Positioned Marine Vessels in Drifting Managed Sea Ice. *Modeling, Identification and Control*, *35*(4), 249-262.

Lau, M. (2006). Discrete Element Modeling of Ship Manoeuvring in Ice. In *Proceedings of the 18th IAHR International Symposium on Ice, Sapporo, Japan* (p. 25-32).

Lau, M. (2011). Ship Manoeuvring-in-Ice Modeling Software OSIS-IHI. In *Proceedings of the International Conference on Port and Ocean Engineering Under Arctic Conditions.*

Lau, M., Lawrence, K. P., & Rothenburg, L. (2011). Discrete Element Analysis of Ice Loads on Ships and Structures. *Ships and Offshore Structures*, *6*(3), 211–221.

Lau, M., & Simões Ré, A. (2006). Performance of Survival Craft in Ice Environments. In *Proceedings of the International Conference and Exhibition on Performance of Ships and Structures in Ice, Banff, Alberta, Canada.*

Leavitt, J. A. (2009). Optimal Thrust Allocation in a Dynamic Positioning System. *Transactions-Society of Naval Architects and Marine Engineers*, *116*, 153–165.

Liu, L., Zhan, D., Spencer, D., & Molyneux, D. (2010). Pack Ice Forces on Floating Offshore Oil and Gas Exploration Systems. In *Proceedings of the International Conference and Exhibition on Performance of Ships and Structures in Ice* (p. 20-23). Anchorage, Alaska, USA.

Løset, S. (1994a). Discrete Element Modelling of a Broken Ice Field – Part I: Model Development. *Cold Regions Science and Technology*, *22*(4), 339–347.

Løset, S. (1994b). Discrete Element Modelling of a Broken Ice Field – Part II: Simulation of Ice Loads on a Boom. *Cold Regions Science and Technology*, *22*(4), 349–360.

Løset, S., Kanestrøm, Ø., & Pytte, T. (1998). Model Tests of a Submerged Turret Loading Concept in Level Ice, Broken Ice and Pressure Ridges. *Cold Regions Science and Technology*, *27*(1), 57-73.

Løset, S., & Timco, G. (1993). Laboratory Testing of a Flexible Boom for Ice Management. *Journal of Offshore Mechanics and Arctic Engineering*, *115*(3), 149–153.

Lubbad, R., & Løset, S. (2011). A Numerical Model for Real-Time Simulation of Ship-Ice Interaction. *Cold Regions Science and Technology*, *65*(2), 111–127.

McKenna, R. F., Spencer, D., Lau, M., Walker, D., & Crocker, G. (1997). Modelling the Forces Exerted by Pack Ice Consisting of Small Floes. In *Proceedings of the International Conference on Offshore Mechanics and Arctic Engineering* (pp. 329–338). Yokohama, Japan.

Mellor, M. (1986). *Mechanical Behavior of Sea Ice*. Springer.

Metrikin, I., Kerkeni, S., Jochmann, P., & Løset, S. (2015). Experimental and Numerical Investigation of Dynamic Positioning in Level Ice. *Journal of Offshore*

Mechanics and Arctic Engineering, *137*(3), 031501.

Metrikin, I., Løset, S., Jenssen, N. A., & Kerkeni, S. (2013). Numerical Simulation of Dynamic Positioning in Ice. *Marine Technology Society Journal*, *47*(2), 14–30.

Michailidis, M., & Murdey, D. C. (1981). Performance of CCGS Franklin in Lake Melville, 1980. In *The Society of Naval Architects and Marine Engineers, Ice Tech Symposium.* Ottawa, Canada.

Millan, J. (2008). *Thrust Allocation Techniques for Dynamically Positioned Vessels* (Tech. Rep. No. LM-2008-04). Institute for Ocean Technology.

Millan, J., & Wang, J. (2011). Ice Force Modeling for DP Control Systems. In *Dynamic Positioning Conference.* Houston, Texas, USA.

Molyneux, D., Spencer, D., Liu, L., & Zhan, D. (2012). Simulation of Ship Performance in Ice Using a Discrete Element Method. In *Proceedings of the Ice Class Ships* (pp. 4–5). London, UK.

Murray, J., & Spencer, D. (1996). Preliminary Investigations into Mooring Forces on a Semisubmersible and a Turret Moored Tanker in Pack Ice, Current and Waves. In *Proceedings of the 15th International Conference on Offshore Mechanics and Arctic Engineering* (Vol. IV, p. 41-54). Florence, Italy.

Murray, J., & Spencer, D. (1997). A Simulation Model for a Turret Morred Tanker in Pack Ice Cover. In *Proceedings of the 14th International Conference on Port and Ocean Engineering under Arctic Conditions (POAC'97)* (p. 135-146). Yokohama, Japan.

Nocedal, J., & Wright, S. (2006). *Numerical Optimization*. Springer Science & Business Media.

Nozawa, K. (1999). A Consideration on Ship Performance in Broken Ice Sea. In *Proceedings of the 9th International Offshore and Polar Engineering Conference.*

Peng, H., & Spencer, D. (2008). Simulation of dynamic positioning of a fpso and

a shuttle tanker during offloading operation. In *The Eighteenth International Offshore and Polar Engineering Conference.*

Quinton, B. (2006). *Decice implementation of ship performance in ice: a summary report* (Tech. Rep. No. SR-2006-06). Institute for Ocean Technology, National Research Council of Canada.

Rohlén, Å. (2009). Relationship Between Ice-Management and Station Keeping in Ice. In *Proceedings of the Dynamic Positioning Conference, Marine Technology Society.* Houston, TX.

Sawamura, J., & Tachibana, T. (2011). Development of a Numerical Simulation for Rotating and Sliding of the Ice Floes along a Ship Hull. In *Proceedings of the International Conference on Port and Ocean Engineering Under Arctic Conditions.*

Sayed, M., & Carrieres, T. (1999). Overview of a New Operational Model. In *Proceedings of the 9th International Offshore and Polar Engineering Conference* (Vol. 2, pp. 622–627).

Schultz, L. A., Middleton, R. W., & Dai, R. (1994). Operational Performance of the RV Nathaniel B. Palmer. In *The 5th International Conference on Ships and Marine Structures in Cold Regions, ICETECH '94.* Calgary, Canada.

SNAME. (1952). Nomenclature for Treating the Motion of a Submerged Body through a Fluid. *New York: Technical and Research Bulletin*, 1–5.

Sørensen, A. J. (2011). A Survey of Dynamic Positioning Control Systems. *Annual Reviews in Control*, *35*(1), 123–136.

Spencer, D., & Molyneux, D. (2009). Predicting Pack Ice Loads on Moored Vessels. In *Proceedings of the International Conference of Ship and Offshore Technology.* Busan, Korea.

Tatinclaux, J.-C. (1984). *Model Tests on Two Models of WTGB 140-Foot Icebreaker*

(Tech. Rep. No. 84-3). Hanover, NH: U.S. Army CRREL.

Turlach, B. (1998). *QuadProg: Functions to Solve Quadratic Programming Problems (Release 1.4).* `http://staffhome.ecm.uwa.edu.au/~00043886/software/quadprog.html`.

Vance, G. P. (1980). *Analysis of the Performance of a 140-Foot Great Lakes Icebreaker: USCGC Katmai Bay* (Tech. Rep. No. 80-8). U.S. Army CRREL.

Vinogradov, O. (1986). Simulation Methodology of Vessel-Ice Floes Interaction Problem. In *Proceedings of the 5th International Conference on Offshore Mechanics and Arctic Engineering, Tokyo.*

Wang, B., Daley, C., Sayed, M., & Liu, J. (2010). Global Ice Loads on Arctic Drillships. In *Proceedings of Icetech, Anchorage, Alaska, USA.*

Williams, J. R., Hocking, G., & Mustoe, G. G. (1985). The Theoretical Basis of the Discrete Element Method. In *Proceedings of the NUMETA 1985, Numerical Methods of Engineering, Theory and Applications.* Rotterdam, The Netherlands.

Wright, B. (2000). *Full Scale Experience with Kulluk Station Keeping Operations in Pack Ice (With Reference to Grand Banks Development)* (Tech. Rep. No. 25-44). Ottawa, Canada: Canadian Hydraulics Centre, National Research Council of Canada.

Zhan, D., Agar, D., He, M., Spencer, D., & Molyneux, D. (2010). Numerical Simulation of Ship Maneuvering in Pack Ice. In *ASME 2010 29th International Conference on Ocean, Offshore and Arctic Engineering* (pp. 855–862).

Zhan, D., & Molyneux, D. (2012). 3-Dimensional Numerical Simulation of Ship Motion in Pack Ice. In *ASME 2012 31st International Conference on Ocean, Offshore and Arctic Engineering* (pp. 407–414).

Zhang, J., & Hibler, W. (1997). On an Efficient Numerical Method for Modeling Sea

Ice Dynamics. *Journal of Geophysical Research: Oceans*, *102*(C4), 8691–8702.

Zhou, Q., Peng, H., & Qiu, W. (2016). Numerical Investigations of Ship-Ice Interaction and Maneuvering Performance in Level Ice. *Cold Regions Science and Technology*, *122*, 36-49.